Pre-print

Malusà, M. G., Resentini, A., & Garzanti, E. (2016).

Hydraulic sorting and mineral fertility bias in detrital geochronology.

Gondwana Research, 31, 1-19.

http://dx.doi.org/10.1016/j.gr.2015.09.002

Hydraulic sorting and mineral fertility bias in detrital geochronology

Marco G. Malusà, Alberto Resentini*, Eduardo Garzanti

Department of Earth and Environmental Sciences, University of Milano-Bicocca, Piazza della Scienza 4, I-20126 Milan, Italy

*Corresponding author. Tel.: +39 02 6448 2071; fax: +39 02 6448 2073
E-mail addresses: marco.malusa@unimib.it; alberto.resentini@unimib.it

ABSTRACT

Detrital geochronology studies require a careful quantification of hydraulic sorting effects, and of the propensity of different parent rocks to yield detrital grains of specific minerals when exposed to erosion (mineral fertility). Because the physical processes of settling and selective entrainment are well known, their effects in sediments can be easily detected and modelled mathematically. By contrast, mineral fertility in parent rocks depends on their full geological history. As a consequence, the relationships between bedrock geology and mineral fertility are hardly predictable, and a direct measurement of this latter parameter is thus required. In this review article, we describe the basic principles of hydraulic sorting, and illustrate a quantitative approach for mineral fertility determination that applies these basic principles to the analysis of modern sediments. Its application to the European Alps shows that apatite and zircon fertility values may range over three orders of magnitude. Variable mineral fertility in parent rocks thus represents, by far, the largest source of bias in detrital geochronology studies. Our study highlights an evident relationship between bedrock geology and mineral fertility, which confirms that the mineral concentration in modern sediments, in the lack of hydraulic sorting effects, is a good proxy of the mineral abundance in bedrock. Mineral fertility maps of the European Alps unravel that metamorphic and plutonic rocks generally have higher apatite and zircon fertility values than sedimentary rocks, but major variations are also observed between different tectonic units within the same paleogeographic domain. The impact of mineral fertility in detrital studies is eventually illustrated with examples from the Alpine region, based on alternative sampling strategies (i.e., the confluence sampling and the along-trunk sampling approaches). We show that geological interpretations are strongly improved when mineral fertility is properly taken into account, not only in modern settings, but also in ancient sedimentary successions.

Keywords: hydraulic sorting; mineral fertility maps; sediment budgets; European Alps

Contents

1. Introduction

Detrital geochronology is increasingly employed in paleotectonic reconstructions and landscape evolution problems. Detrital studies require a careful evaluation of the effects induced by hydraulic sorting, and by the variable propensity of different parent rocks to yield detrital grains of specific minerals when exposed to erosion (mineral fertility - Moecher and Samson, 2006). Mineral fertility in bedrock controls the weight concentration of datable mineral grains in detritus, and represents a major source of bias that is potentially introduced whenever the results of single-mineral analyses are extrapolated to bulk-sediment fluxes (Dickinson, 2008; Hietpas et al., 2011a). Such “mineral fertility bias” has a major impact on estimated sediment budgets and erosion patterns (e.g., Brown et al., 1995; Amidon et al., 2005a; Brewer et al., 2006; Tranel et al., 2011), larger than any other source of bias affecting detrital geochronology datasets (Malusà, 2014). Nevertheless, the effects of hydraulic sorting (e.g., Malusà et al., 2013) and of variable mineral fertility (e.g., Brewer et al., 2006; Spiegel et al., 2007; Champagnac et al., 2014) are seldom considered in detrital studies, leading to geological interpretations that are prone to be incorrect.

In this review article, we illustrate the basic principles of hydraulic sorting, and a quantitative approach for mineral fertility determination that applies these basic principles to the analysis of

modern sediments, in order to get key information for the geochronological analysis of sedimentary successions of any age. Specifically designed for routine application in detrital geochronology, this approach is applied here to the European Alps, and provides estimates of mineral fertility that can be used to extrapolate the results of grain-age distributions to bulk sediment. Erosion patterns can be thus deduced from simple unmixing of single-mineral geochronological signals. The implications for the analysis of orogenic erosion are eventually illustrated with examples based on geochronological analyses of detrital zircon and apatite, and on alternative sampling strategies.

2. Current approaches to mineral fertility

Detrital samples derived from the mixing of geochronologically distinct detrital sources (A and B in Fig. 1) are expected to yield polymodal grain-age distributions that include different grain-age populations (Bernet et al., 2004; Bernet and Garver, 2005; Resentini and Malusà, 2012). The relative size (*n, m*) of different populations depends (i) on the relative size of the catchment areas, (ii) on the erosion rate in each catchment, and (iii) on the mineral fertility of the parent bedrock. If we know two of these factors, then we can calculate the third. Common practice is to assume mineral fertility changes as negligible (He et al., 2014), in order to calculate relative erosion rates directly from the relative size of grain-age populations, sometimes additionally weighed by the relative drainage areas (Fig. 1, case 1) (Malusà et al., 2009a; Zhang et al., 2012; Glotzbach et al., 2013; Saylor et al., 2013). However, whole rock geochemical analyses from North America granitoids suggest that zircon fertility values may vary by a factor of 5 even in similar lithologies (Moecher and Samson, 2006; Dickinson, 2008). The constant-fertility assumption is thus untenable, and even more so when considering a wide range of rock types (Fig. 1, case 2) (e.g., Fedo et al., 2003; Hietpas et al., 2011a). In the lack of a proper quantification, the impact on geological interpretations may be huge, as shown by the contrasting erosion patterns obtained in cases 1 and 2 of Fig. 1.

In order to solve this problem, the volume frequency of the target mineral in the source rocks has been either evaluated by point counting under the microscope (e.g., Silver et al., 1981; Tranel et al., 2011), or by adopting a geochemical approach (Cawood et al., 2003; Dickinson, 2008). The geochemical approach to zircon fertility proposed by Dickinson (2008) uses the zirconium (Zr) content derived from whole-rock geochemical analyses as a proxy for zircon content (volume % zircon ≈ 1.15 wt.% Zr, assuming that Zr is exclusively host in zircon). A zircon fertility factor (ZFF), assigned according to the Zr content in each rock (e.g., ZFF=1.0 for subduction-related granitoids having ~150 ppm Zr, and ZFF=3.5 for Grenville granitoids having ~520 ppm Zr; Dickinson, 2008), is employed to weigh the size of grain-age populations in samples of mixed

provenance, in order to estimate the relative contributions of different bedrock sources to the final sediment.

Such a geochemical approach to mineral fertility is seldom applicable in detrital studies, and is prone to introduce further unquantifiable bias. In fact: (i) bedrock data for comparison are not available in most of the cases, or are restricted to few and/or poorly representative rock types; (ii) Zr is found not only in zircon, but also in other rare minerals (xenotime, baddeleyite) and in rock fragments (e.g., volcanic glass); (iii) zircon grains too small in size for dating, or hosted as inclusions in other minerals (e.g., in biotite), are improperly included in the estimate. This precludes routine application of geochemical analysis to mineral fertility estimates, and implies that geochemical data, when available, provide only an upper threshold for effective zircon fertility values.

An alternative approach to mineral fertility determination is thus required. The method illustrated in this article is based on a rather simple consideration: if a rock is crushed and its fragments get finer downstream because of pure mechanical grinding without significant modifications during transport and deposition, the sediment composition should reflect bedrock composition exactly. Therefore, in a temperate/cold climate where chemical weathering is minor, mineral fertility in the source rocks can be effectively determined by measuring the mineral content in the sediment they produce, provided that a range of potential sources of bias are properly accounted for and minimized. Specifically, this approach requires that no significant modification has been induced by hydrodynamic processes in the natural environment, and that no bias is introduced subsequently during mineral separation in the laboratory. The first requirement can be tested by a proper application of the basic principles of hydraulic sorting, which are illustrated in section 3. The second requirement can be met by a proper methodological approach to mineral separation, as illustrated in section 4.

Figure 1

3. Basic principles of hydraulic sorting

3.1 Settling velocity and intrasample mineralogical variability

Tractive currents sort detrital grains during transport and deposition according to their size, density and shape (Schuiling et al., 1985; Komar, 2007). Grains with the same settling velocity are deposited together. Because grain shape has a major impact on settling only for phyllosilicates, low-density minerals like quartz and feldspars are associated in sorted sediments with significantly smaller ultradense minerals, such as zircon and monazite (principle of hydraulic equivalence; Rubey, 1933) (Fig. 2A). The difference in size between settling-equivalent minerals is called the "size shift", and is generally referred to quartz (Rittenhouse, 1943; Garzanti et al., 2008).

Settling velocity of a detrital grain in a fluid (Fig. 2B) reflects the balance between the gravitational force (F_G) and the drag resistance due to turbulence (F_T) and viscosity (F_V). Turbulence controls settling of pebbles, as described by the Impact Law, whereas viscosity controls settling of clay and silt-sized grains, as described by the Stokes' Law (Fig. 3A). In water-laid sand, settling velocity is controlled by both viscosity and turbulence, and several empirical formulas can be used to predict theoretical size-shift values (e.g., Cheng, 1997; Fig. 3B). Size-shifts in sand increase with grain size according to a sigmoidal function from those predicted by the Stokes' law to those predicted by the Impact law, and also increase with mineral density (Fig. 3A). In minerals relevant for detrital geochronology, empirical size-shift values range from 0.2-0.35ϕ for apatite to 0.65-1.2ϕ for monazite. Micas, due to their platy shape, settle slower than quartz despite their higher density (e.g. Komar et al., 1984; Le Roux, 2005), yielding empirical size-shift values between -0.1 and -0.2 ϕ (Garzanti et al., 2008; Fig. 3B).

As an effect of size-density sorting during settling, bedload sediments display a strong intrasample compositional variability among grain-size classes, which can be modelled mathematically. MinSORTING (Resentini et al., 2013) is an Excel worksheet specifically conceived for this purpose, and calculates the size-shift predicted for each mineral by the appropriate formula (Stokes' for silt, Cheng's for sand, Impact for gravel) and its distribution in different grain-size classes. Fundamental input parameters are the fluid type and the mean grain-size and sorting values of the bulk sediment, which can be easily obtained by sieving. The good fit between observed and modelled distributions, despite mineral grains are considered as perfect spheres, indicates that the effect of grain shape on settling is negligible for most of the minerals (Fig. 3C). The modelling approach applied to bedload sediment could be ideally exported to the analysis of suspended load in transit, even though the settling-equivalence analysis is more complex for suspended load. In fact, suspended load consists of a ternary mixture of clay, silt and sand modes (e.g., Garzanti et al., 2011) and the settling-equivalence principle applies to each. The behaviour of platy minerals such as micas, largely employed in detrital geochronology (e.g., Najman et al., 1997; Carrapa et al., 2004; Hodges et al., 2005) and chiefly transported as suspended load, is thus more difficult to predict.

3.2 Selective entrainment and intersample mineralogical variability

Modern bulk-sediment samples with identical provenance may display significant intersample compositional variability generated by the easier entrainment of larger lower-density minerals by tractive currents (Komar, 2007). Larger minerals project higher above the bed and hence experience greater flow velocities and drag forces (Fig. 2C). Moreover, they have smaller pivoting angles (α in Fig. 2C) than settling equivalent smaller and denser minerals (Komar and Li, 1988). As a consequence of selective entrainment, lag deposits are enriched in denser minerals to various degrees, and placer deposits eventually form. In placers, ultradense minerals such as garnet, zircon, rutile, monazite and

magnetite are enriched by an order of magnitude or more relative to the original sediment (Reid and Frostick, 1985; Slingerland and Smith, 1986), leading to a remarkable change in colour and density (reddish and 3.5-4.0 kg/dm^3 in garnet placers, black and >4.0 kg/dm^3 in magnetite placers).

The composition of placer lags cannot thus be used to directly infer the composition of parent bedrock. For this purpose, the compositional effects of selective entrainment have to be first removed by SRD correction (Garzanti et al., 2009), i.e., by iteratively correcting the relative abundances of detrital minerals as determined by point-counting under the microscope in proportion to their densities, until the expected grain density of the bulk sample is restored (Resentini et al., in prep.). The greatest is the compositional modification induced by selective entrainment, the largest is the uncertainty introduced by this kind of procedure.

3.3 Size-density sorting and chemical variability

Chemical elements are preferentially contained in specific minerals having different density and/or shape (e.g., Rb in slow-settling platy mica, Zr and Hf in fast-settling ultradense zircon). Therefore, hydrodynamic processes that control mineralogical variability in sediments also control their chemical variability (McLennan et al., 1993). In detritus, elements hosted in tectosilicates (Si, Na, Ca, Sr) are thus expected to be enriched in the central part of the grain-size distribution, those hosted in micas and associated inclusions to be enriched in the coarse tail, and those chiefly hosted in ultradense minerals to be concentrated in the fine tail (Garzanti et al., 2010). Among common ultradense minerals, zircon typically contributes most of Zr, Hf and significant amount of Yb, Lu, U, Ta, and Pb; monazite and allanite much of LREE and Th; xenotime much of Y and HREE. As a result, the finest grain-size classes of a given sediment sample might be two or three orders of magnitude richer in REE, Th, Zr and Hf than the coarsest classes, as a simple effect of size-density sorting during deposition. By contrast, strong enrichment of these elements in the bulk sediment may indicate compositional modifications due to selective entrainment, with placer lags showing enrichments by orders of magnitude relative to neutral bedload and UCC. Potential bias induced by anthropogenic activities (e.g., an increase in P due to fertilizers) can be easily recognized, because anthropogenic bias is expected to produce a mismatch only for selected elements, rather than for the whole range of elements hosted in ultradense minerals (Resentini and Malusà, 2012).

Figures 2, 3

4. Procedure for mineral fertility determination

In order to measure mineral fertility in catchment bedrock starting from the analysis of a sample of river sediment, we can follow the simple procedure synthesized in Fig. 4. A sample of

sorted bedload sand is quartered in the laboratory and dry sieved at 1ϕ intervals. The resulting grain-size distribution is plotted as a cumulative frequency curve (Fig. 5A) to determine the distribution percentiles (ϕ_n), and to calculate the mean grain size (D_m) and sorting value (σ) of the bulk sediment (step A1).

Grain density of the bulk sample is measured on a quartered fraction using a hydrostatic balance (step A2). We weigh the sample first in air and next immersed in water, taking care to wet grains before immersion and avoid floating due to surface tension. Grain density is calculated as:

$$\delta_{sediment} = W_{in\ air} / (W_{in\ air} - W_{in\ water}) \cdot \delta_{water} \qquad (1)$$

where δ_{water} is 0.9982 kg/dm^3 at 20°C, and W is the weight of the sample (Pratten, 1981). Grain density can be be determined separately for the 63-250 μm and the 250-2000 μm grain-size classes in order to reduce errors related to incomplete elimination of interstitial air, and the results are then weighed by the weight percentage of each grain-size class as determined by sieving.

Then, we model the distribution and sorting of minerals in different grain-size classes with MinSORTING (Resentini et al., 2013) (step A3), using as input parameters the mean grain size and sorting calculated in step A1, and the relative exposure area of rocks ascribed to different end-member compositions, as calculated on geological maps by GIS. Modelling allows us to choose the most suitable size windows to maximize the recovery of the target mineral during separation (step A4), and mathematically predict the fraction falling outside the chosen grain-size range (Fig. 5B-D). In ideal conditions, most of the target mineral is concentrated in a narrow size window, and the amount of mineral measured after separation is close to the total amount in the bulk sediment. For instance, in a fine-grained and very well sorted sand with a typical subducted-axial-belt modal composition (Fig. 5B), we expect to recover virtually all apatite and zircon grains in the 63-250 μm size window. However, ideal conditions are not the rule. In poorly-sorted samples, the mineral amount lost in fractions finer or coarser than the chosen size window is much larger than in well-sorted samples (Fig. 5C). If the analysed size-window is not correctly chosen with respect to both sample grain-size and mineral size-shift, most of the target mineral may be lost during separation, despite its original presence in the sediment sample (Fig. 5D).

Within the selected size window, we perform a hydrodynamic pre-concentration of the dense fraction using a Gemeni shaking table (step A5). Shaking tables exploit the basic principles of size-density sorting illustrated in section 3. Therefore, in order to effectively concentrate detrital grains according to their density, we process different grain-size classes separately to minimize the effect of grain size (Malusà et al., 2013). Dense fractions recovered after hydrodynamic pre-concentration are than merged together, and further purified by centrifuging in sodium polytungstate diluted at 2.90

kg/dm^3. The dense fraction (> 2.90 kg/dm^3) is recovered by freezing in liquid nitrogen, and weighed with a high-precision balance. The dense mineral concentration for the selected size-window is thus obtained (step A6). If the analyzed size window is sufficiently large and centered on the mean grain size, the obtained value of dense mineral concentration is representative of the sample as a whole.

The set up of step 7 may vary according to the physical properties of the target mineral. If we want to retrieve apatite and zircon, the dense fraction is further refined with a Frantz magnetic separator under increasing field strength, and using a proper side and forward slope of the tray to remove magnetic minerals without affecting apatite and zircon (Sircombe and Stern, 2002). The dense diamagnetic fraction is passed in glassware through liquid diiodomethane (3.32 kg/dm^3), to split minerals denser than 3.32 kg/dm^3 (including zircon, ~4.65 kg/dm^3) and minerals having densities ranging between 2.9 and 3.32 kg/dm^3 (including apatite, ~3.2 kg/dm^3). Quantities before and after each separation step are carefully weighed to detect any potential loss of material during processing. The percentage of apatite and zircon in these concentrates, which also include other diamagnetic heavy minerals such as kyanite and barite, is determined by point counting under the microscope, possibly on the same slides prepared for geochronologic analyses (step A8). The apatite and zircon concentration for the selected size-window is thus obtained. We add to these values the amount of mineral which is expected to be lost in the coarser and finer grain-size classes, as modelled by MinSORTING, to obtain the apatite and zircon concentration for the bulk sediment (step A9). Undatable grains (e.g., smaller than 63 μm for optical analyses) are not included in this calculation.

The mineral concentration retrieved after step A9 is equal to mineral fertility in the source rocks only if sediment composition was not significantly modified by selective entrainment effects. We test the analyzed samples for anomalous concentration (or depletion) of denser grains (step A10) by comparing the bulk grain density and the dense mineral concentration measured during step A2 and step A6 with reference values in eroded bedrock, which are compiled in Fig. 6A. Density of upper crustal rocks (SRD in Fig. 6A) generally lies in a narrow range of 2.70±0.05 kg/dm^3, and may reach above 2.80 kg/dm^3 only in mafic/ultramafic igneous or metamorphic rocks (e.g., ophiolites). Higher values in sediment points to hydraulic concentration of denser grains by selective entrainment (Fig. 6B). Also the abundance of heavy minerals in a particular source rock is a function of its density (HMC in Fig. 6A). In the lack of hydraulic effects, dense mineral concentration in detritus is generally <10%, although it may reach values as high as 15-20% in sediments derived from magmatic arcs and ophiolites (Garzanti and Andò, 2007b). Higher values, in grain-size windows sufficiently representative of the bulk sediment, point to significant modifications of sediment composition by selective entrainment effects (Fig. 6B).

Any compositional modification induced by selective entrainment should be considered in mineral fertility calculations, and eventually removed by SRD correction. This correction requires a full modal compositional characterization of the analyzed sample, either under the optical microscope or by QEMSCAN analyses.

Figures 4, 5, 6

5. The European Alps study area

5.1 Tectonic setting

The European Alps are an arcuate orogen chiefly developed during the Cretaceous-to-Paleogene subduction of the Tethyan ocean and the European paleomargin beneath the Adriatic microplate (Dewey et al., 1989; Schmid et al., 2008; Handy et al., 2010; Malusà et al., 2011a; Zhao et al., 2015). The NE part of the orogen consists of Adria-derived Austroalpine and Southalpine units, accreted against the upper plate (i.e., Adria) in Cretaceous times during the early stages of the Alpine orogeny (Zanchetta et al., 2012; Malusà et al., 2015a,b). This Cretaceous wedge forms a tectonic lid on top of the Cenozoic metamorphic units, and is intruded by Paleogene magmatic rocks (von Blanckenburg et al., 1998; Rosenberg, 2004; Malusà et al., 2011b).

The underlying metamorphic units record the Paleogene subduction and exhumation of attenuated European crust and adjoining ocean-continent transition. In the Central Alps, the Paleogene metamorphic units include the deepest levels of the post-collisional nappe stack (Argand, 1911), represented by the amphibolite-facies Lepontine gneisses (Merle et al., 1989). In the Western Alps, a belt of Eocene eclogite units (Eclogite belt in Fig. 7) is exhumed at the rear of a double-vergence accretionary wedge (Frontal wedge in Fig. 7), which includes blueschist-to-greenschist-facies cover sequences and basement slivers (Malusà et al., 2011a), whereas continental crust escaping major Alpine metamorphism crops out in the External Massifs on the European mainland.

In the Ligurian Alps, the Eclogite belt and the Frontal wedge are partly buried beneath the wedge-top successions of the Tertiary Piedmont Basin (Mutti et al., 1995; Gelati and Gnaccolini, 2003). Farther east, along the Alps-Apennines transition zone, the Alpine orogenic wedge includes the Ligurian units of the Northern Apennines, largely structured within the framework of Alpine subduction and topped by Epiligurian successions (Catanzariti et al., 2002; Cerrina Feroni et al., 2004). The underlying Subligurian and Tuscan units were instead accreted since the Oligocene during Adriatic subduction beneath the European plate. They include Meso-Cenozoic successions topped by Oligo-Miocene turbidites fed from the exhuming Lepontine dome (Garzanti and Malusà, 2008), originally deposited in the Adriatic foredeep and now exposed through tectonic windows carved in the Ligurian units (Elter et al., 1999). The orogenic wedge of the Northern Apennines

underwent subsidence during most of its Cenozoic evolution, and was long buried by detritus eroded from the Alps, to be finally uplifted and exhumed in Plio-Quaternary times (Malusà and Balestrieri, 2012). Huge amounts of Alpine detritus were thus recycled and transferred into the Po Plain, which represents at the same time the proforeland basin of the Apennines and the retroforeland basin of the Alps.

5.2. Sampling strategy

For apatite and zircon fertility measurements, we analyzed 40 samples of sorted bedload sediment collected from Alpine tributaries at the exit of major valleys (F1-F40), and 13 samples collected within the adjoining plains (S1-S13) (details in supplementary Table S1). We applied to all of these samples the whole procedure for mineral fertility determination described in section 4 (steps A0 to A10), which was integrated by additional chemical analyses (steps B1 and B2 in Fig. 4).

Chemical analyses were carried out on the sieved sand fraction (63-2000 μm), pulverized in agate jar, at ACME laboratories, Vancouver. After lithium metaborate/tetraborate fusion and nitric acid digestion, major oxides and minor elements were determined by ICP emission spectroscopy, and trace elements by ICP-MS. This allowed us to obtain independent upper thresholds for mineral fertility values, assuming that all of the Zr and P is contained in zircon and apatite, respectively. We also used chemical analyses as an additional test for selective entrainment effects (i.e., by checking samples for anomalous concentrations of elements that are chiefly hosted in ultradense minerals).

In order to further test the reliability of our mineral fertility measurements, and quantify the bias introduced by (i) the choice of detrital pulses of slightly different age and (ii) the subjective choices of sampling location and collected grain size in the sample spot, we integrated the dataset with a few replicate samples and performed replicated measurements (details in supplementary Table S4). The samples chosen in this perspective include: two samples from a quarry of Pleistocene sand, consisting of point-bar deposits ascribed to distinct detrital pulses in the paleo-Dora Baltea river; two modern sands collected from distinct distributary channels of the Po delta; two modern sands collected 4 km apart along the Dora Baltea river trunk. These latter samples also allowed us to test the impact of sampling different facies, by comparing the results yielded by point bar deposits and those yielded by nearby overbank deposits, which include sediment transported as suspended load.

Samples were checked for any possible relationship between mineral fertility and grain-size parameters. The obtained mineral fertility values were finally reported in mineral fertility maps for apatite and zircon, in order to discuss their relationships with the geology of eroded bedrock.

Figure 7

6. Results

The apatite and zircon concentrations measured in samples F1 to F40, according to the procedure of Fig. 4, span over three orders of magnitude. Apatite concentration values range between 10^1 and $>10^3$ ppm. Zircon concentration values range between 10^{-1} and 10^2 ppm. Such values show no apparent correlation with the mean grain size and sorting of the analyzed bulk sediment (Fig. 8A). This excludes any prominent control of grain size parameters on measured mineral concentration. Grain density values and dense mineral concentrations in these samples indicate negligible selective entrainment effects (Fig. 8B). Grain density values are sistematically $\leq$ 2.7 kg/dm^3, with slightly higher values in samples draining lower crustal rocks (e.g., F21 and F22). Dense mineral concentration is much lower than 10%. Therefore, the mineral concentrations reported in Figure 8A can be safely considered as representative of the mineral fertility values in eroded bedrock.

It is worth noting that the variability in mineral concentration for replicate measurements (Fig. 9) is well below the variability of three orders of magnitude documented for mineral fertility in bedrock. This is true not only when considering minor variations in sample location and age of detrital pulses, but also in the extreme case of inaccurate sampling of different facies (case A2, i.e., overbank deposits including sediment transported as suspended load).

Although we have analyzed on average only 40% of the bulk sediment in each sample, by following the procedure illustrated in figure 4 we estimate to have retrieved on average more than 55% of the total apatite, and more than 65% of the total zircon grains contained in each sample (supplementary Table S2). We underline that a correct choice of the size window is crucial for this kind of analysis, and that using the dense mineral concentration as a test for selective entrainment can be misleading in the case of an incorrect choice of the analyzed size window. This is illustrated by the example of sample F33, which yielded dense mineral concentration >80% because the analyzed size window only included the finest tail of the grain-size distribution (Fig. 8B). Therefore, the extreme dense mineral concentration in sample F33 is a simple effect of size-density sorting during settling (see section 3.1), as confirmed by the grain-density value (<2.7 kg/dm^3) measured in the bulk sample. This example demonstrates that grain density measurements of the bulk sediment provide a more robust test for selective entrainment than dense mineral concentration values, when they are based on the analysis of specific (and narrow) grain-size classes.

Bulk sediment geochemistry (Fig. 8C) supports the results of figure 8B. Elements chiefly hosted in ultradense minerals show in fact concentrations very close to UCC (Taylor and McLennan, 1985; 1995), providing no evidence for selective entrainment effects in the analyzed samples (see supplementary Table S3 for further details). The only outlier is sample F33 (dashed line in Fig. 8C), including detrital grains derived from the erosion of mantle rocks (Voltri unit, VO in Fig. 7) and thus

not comparable to UCC. Moreover, bulk-sediment geochemical analyses provided an upper threshold for zircon and apatite fertility values (thin yellow lines in Fig. 10), assuming that Zr and P_2O_5 are exclusively hosted in zircon and apatite, respectively. Unlike mineral fertility values, geochemical threshold values are rather constant (~10^2 ppm for zircon, and ~10^3 ppm for apatite) and intersample variations are confined within one order of magnitude, instead of three orders of magnitude as observed for mineral fertility. Mineral fertility values are invariably lower than the corresponding upper thresholds provided by bulk-sediment geochemical analyses, as indeed expected (Fig. 10). The diagrams in figure 10 also show that the observed variability in mineral fertility markedly decreases when the results are analyzed within homogeneous orogenic segments. The highest mineral fertility values are thus found in the Central Alps and in the External Massifs (zircon ~10^0-10^1 ppm; apatite ~10^1-10^3 ppm), whereas the lowest values are found in the Southern Alps and in the Alps-Apennines transition zone (zircon ~10^{-1}-10^0 ppm; apatite ~10^1 ppm). A higher variability in mineral fertility values is observed in the axial Western Alps, even though the geochemical upper thresholds in this orogenic segment are still rather constant. The difference between measured and geochemically-inferred fertility values, i.e., the vertical distance between the thin and the thick lines in figure 10, is a measure of the amount of Zr and P_2O_5 that is either found in minerals other than zircon and apatite, or as inclusions in other mineral grains. Such a vertical distance is lowest in the Central Alps, and greatest in the Southern Alps and in the Alps-Apennines transition zone.

In the lack of selective entrainment and other hydraulic effects (see Fig. 8), we can assume that the analyzed detrital samples are fully representative of the eroded bedrock. This implies that the mineral fertility values measured in detrital samples can be safely used to produce bedrock fertility maps for the chosen minerals (i.e., apatite and zircon). These mineral fertility maps are shown in figure 11, and report the average mineral fertility values in each sub-basin upstream the analyzed samples. Such fertility values are rather constant in subbasins draining the same tectonic unit, which points to a prominent geological control on mineral fertility. As a consequence, the fertility ranges found in specific tectonic units were extrapolated in these maps outside the analyzed subbasins, and the resulting picture was eventually cross-checked using the mineral concentration values measured in the lowland river samples.

Figures 8, 9, 10,11

7. Discussion

We have shown in figure 1 that the constant fertility assumption is untenable. The impact of variable mineral fertility on geological interpretations is in fact major, even if mineral fertility variations are confined within one order of magnitude range.

The direct measurement of mineral fertility in the European Alps unravels that variations in mineral fertility may span over three orders of magnitude (Figs. 8-11). Therefore, the potential impact of variable mineral fertility on detrital geochronology studies, and in particular on sediment budgets based on the deconvolution of grain-age distributions, is huge. When polymodal grain-age distributions are deconvolved into different grain-age populations, the size of each population may vary between 0 and 100%, but only populations representing 5 to 10% of the total distribution can be safely distinguished (Vermeesch, 2004). The expected size variations among different grain-age populations thus range within one order of magnitude only, which is much lower than the three orders of magnitude variations documented for mineral fertility in bedrock (Fig. 11). We can thus conclude that the variable mineral fertility in bedrock represents, by far, the major control and potential source of bias in any sediment budget based on detrital geochronology.

Although independent fertility measurements in subbasins draining the same tectonic unit yielded rather homogeneous values, major variations can be observed between tectonic units ascribed to the same paleogeographic domain. This is, for instance, the case of the Dora-Maira and Gran Paradiso Internal Massifs (DM and GP in Fig. 7), both formed by subduction and eclogitization of European continental crust during the Paleogene. Apatite fertility values are systematically lower in the Dora-Maira (100-200 ppm) than in the Gran Paradiso (400-700 ppm), and similar variations are also observed for zircon (DM = 0.4-1.2 ppm; GP = 5-8 ppm).

Major variations in mineral fertility values are also observed between different External Massifs, representing unsubducted segments of European continental crust with variable proportions of Paleozoic intrusives and metamorphic country rocks. Apatite fertility values systematically decrease towards the south from the Aar-Gotthard (~500 ppm) to the Mont Blanc (~200 ppm) and the Pelvoux-Belledonne Massifs (25-50 ppm), but the highest values (~950 ppm) are found in the Argentera Massif, which is dominated by high-grade metamorphic rocks. On the other hand, zircon fertility values are much lower in the Aar-Gotthard Massif (~5 ppm) than in the Mont Blanc Massif (~100 ppm), and major differences in zircon fertility are also observed between the Pelvoux-Belledonne Massifs (~3-16 ppm) and the Argentera Massif (~80 ppm).

In general terms, the maps in figure 11 show that units chiefly consisting of metamorphic and plutonic rocks have higher apatite and zircon fertility than units largely consisting of sedimentary rocks. In the European Alps, the highest apatite fertility (300-2600 ppm) is found in the Lepontine dome of the Central Alps. Within this composite dome of medium-to-high grade metamorphic rocks, apatite fertility is higher in the eastern (Ticino) subdome (1000-2600 ppm) than in the western (Toce) subdome (300-1000 ppm). This distribution mirrors the shape of the metamorphic isograds recognized in the Lepontine area (Fig. 7). A similar pattern is also observed for zircon

fertility, that is higher in the Ticino subdome (60-70 ppm) than in the Toce subdome (~10 ppm). However, very high zircon fertility characterizes not only the Lepontine gneisses (LD in Fig. 7), but also the migmatitic country rocks and the encased intrusives of the Mont Blanc and Argentera Massifs (80-100 ppm, MB and AR in Fig. 7), and the Permo-Carboniferous continental metasediments of the Houiller unit (50-90 ppm, HO in Fig. 7).

The lowest apatite and zircon fertility values are found instead in the cover successions of the Southern Alps (apatite = 10-30 ppm; zircon = 0.5-6 ppm) and in the sedimentary to very-low-grade tectonic units of the Alps-Apennines transition zone (apatite = 17-95 ppm; zircon = 0.5-7 ppm). In this latter area, zircon fertility is lower to the west, where Ligurian units are dominant (LI in Fig. 7), and slightly higher to the east where wedge-top Epiligurian successions and foredeep turbidites are largely exposed. Because these foredeep turbidites were chiefly fed from the erosion of the exhuming Lepontine dome (Garzanti and Malusà, 2008), and ultrastable species such as zircon are not selectively dissolved during diagenesis (e.g., Morton, 1984; Morton and Hallsworth, 2007), the second-cycle sediments shed from the Apennines should display higher zircon concentrations than the first-cycle sediments shed from the Central Alps, unlike instead observed.

Apatite fertility in plutonic rocks is not exceptionally high. This is illustrated by the Southern Alps example, where a sample draining the largest Alpine intrusive (Adamello, sample F9) yielded the same fertility value as the sand samples draining its country rocks exclusively (F7 and F8). Such findings are confirmed by a comparison between the Mont Blanc and the Argentera External Massifs. Apatite fertility is lower in the Mont Blanc Massif, dominated by Upper Paleozoic intrusives, than in the Argentera Massif, dominated by Early Paleozoic migmatites. Zircon fertility, instead, is possibly higher than average in plutonic rocks, as indicated by the sample draining the Adamello intrusive in the Southern Alps, which yielded a higher zircon fertility value (~6 ppm in sample F9) than the samples draining the Adamello country rocks exclusively (< 1 ppm in samples F7 and F8).

This indicates that apatite crystals in plutonic rocks are generally too small, and included chiefly in larger minerals such as feldspar (e.g., Harrison and Watson, 1984) even in detritus. Their detrital geochronology analysis is thus precluded. In metamorphic rocks, apatite is stable through a wide range of metamorphic facies, and in different protoliths (Spear and Pyle, 2002). Textural features are thus of primary importance in determining the apatite fertility of metamorphic rocks. Most of the apatites in low grade metamorphic rocks are possibly found as inclusions in other poikiloblastic minerals. In medium-to-high grade metamorphic rocks, instead, a higher amount of relatively large apatite grains may grow during regional metamorphism, thus contributing to apatite fertility for

detrital geochronology purposes, as suggested by the high fertility values found in the Lepontine dome (Fig. 11).

The evident relationships between bedrock geology and observed mineral fertility distribution prove that, in the lack of hydraulic sorting effects, the mineral concentration in modern sediments is a good proxy of the mineral fertility in bedrock. However, these relationships are complex, and depend not only on lithology, but also on the whole magmatic, sedimentary or metamorphic evolution of the eroded bedrock. For these reasons, the relationships between bedrock geology and mineral fertility are hardly predictable, and direct measurements of mineral fertility are consequently required.

8. Application to sediment budgets

The impact of variable mineral fertility of source rocks in detrital studies is illustrated here with examples from the European Alps. In these examples, partitioning of mineral contribution for sediment budget calculations are based on alternative sampling strategies, hereafter referred to as confluence sampling and along-trunk sampling approaches (Fig. 12)

The confluence sampling approach (Fig. 12A) requires samples both from major tributaries (S_A and S_B) and from the trunk river downstream of their confluence (S_{A+B}) (e.g., Amidon et al., 2005b; Garzanti et al., 2012). Partitioning is based on a linear combination of grain-age distributions upstream of the confluence (blue and red cumulative curves in Fig. 12A)

$$F_m(x) = \Sigma\ \pi_j\ F_j(x) \qquad (2)$$

where the unknown mixing proportions π_j of the j^{th} component of the mixture are all positive and their sum is 1. The best-fit solution is defined by those values of π_j that minimize the misfit between the modelled distributions $F_m(x)$ and the empirical grain-age distribution observed downstream the confluence (in black). The goodness of fit can be evaluated using the Kolmogorov-Smirnov statistics (parameter $D_{n,n'}$ in Fig. 12A) (e.g., Dunkl and Székely, 2002; Malusà et al., 2013; Vermeesch, 2013), whereas a two-sample Kolmogorov-Smirnov test can be used to check preliminarly whether grain-age distributions upstream of the confluence are statistically different, thus avoiding meaningless linear combinations. This approach requires at least three samples at each node. It allows a direct measurement of mineral fertility in each subbasin, and does not require any independent information on the geochronological fingerprint of parent bedrock.

The along-trunk approach (Fig. 12B) (e.g., Hietpas et al., 2010; Dhuime et al., 2011) can be instead employed when a river cuts across rock units with distinct and not overlapping geochronological signatures (e.g., Resentini and Malusà, 2012), so that grain ages can be used to inequivocally discriminate the provenance of detrital grains. Partitioning according to the along-

trunk approach is based on the deconvolution of grain-age distributions in individual age components of specific size (*m* and *n*). Bias is potentially introduced during partitioning because different parent distributions (e.g., Gaussian, Laplacian, log-normal) can be assumed for deconvolution into best-fit peaks (e.g., Brandon, 1996; Dunkl and Székely, 2002), and because smaller peaks can be eventually missed if the analyzed samples are not large enough (Vermeesch, 2004; Andersen, 2005). Provided that geochronologic ages on bedrock are independently known and well discriminated, only two samples (S_A and S_{A+B}) are needed for unmixing the geochronological signals and characterizing two subbasins in terms of mineral fertility. Fertility of subbasin A (F_A) is directly measured, fertility of subbasin B (F_B) is calculated instead by the formula reported in Fig. 12B (see Appendix 1 for details) .

8.1. Examples based on the confluence sampling strategy

Examples based on confluence sampling within the Po drainage are illustrated in figures 13 and 14. In these examples, we used a dataset of detrital zircon U-Pb ages published in Malusà et al. (2013), which is based on LA-ICPMS analyses systematically performed on zircon grain rims.

Because the sediment budgets in figure 14 are based on lowland samples (see Fig. 7), the analyzed sediments have thus experienced long-distance transport in the plain, and are more prone to mechanical abrasion during transport than samples collected from valley mouths (F1-F40 in Fig. 7). For these reasons, the vulnerability of the dataset to hydraulic sorting and mechanical abrasion must be carefully tested (Fig. 13). As shown in figure 13A, the grain-age distributions in different grain-size classes are statistically indistinguishable, which means that the observed distribution is hardly affected by hydraulic sorting effects. Moreover, the relative abundance of U-rich grains in different U-Pb age populations does not change across the plain (Fig. 13B), as well as the relative abundance of rounded zircon grains (Fig. 13C). This indicates that metamict grains are largely unaffected by mechanical abrasion during fluvial transport, and that rounding during single river transport is not able to selectively remove the outer rims of zircon grains, which would introduce a bias in the analyzed dataset (Malusà et al., 2013). Therefore, the dataset can be safely employed to perform the sediment budgets shown in figure 14.

The example 1 (Fig. 14A) constrains the modern erosion pattern in the Lepontine dome by comparing the modern sediment contributions from the eastern (Ticino) and the western (Toce) subdomes. Sample S_A (Ticino@Bellinzona, F3 in Fig. 7) and sample S_B (Toce@Masera, F1 in Fig. 7) are linearly combined, and compared with sample S_{A+B} collected downstream their confluence (Ticino@Bereguardo, S6 in Fig. 7). The best fit solution is obtained for S_A=44%. However, because the zircon fertility is much higher in the eastern subdome (68 ppm) than in the western subdome (12 ppm), the sediment contribution from the eastern subdome is strongly overestimated if differences

in zircon fertility are not properly considered. When zircon fertility is included in the calculation, the sediment contribution from the eastern subdome is reduced to 12% (yellow star in Fig. 14B), in line with the indications provided by the analysis of cosmogenic nuclides (e.g., Wittmann et al., 2007) and by low-temperature thermochronology (e.g., Garzanti and Malusà, 2008).

The example 2 (Fig. 14C) illustrates a sediment budget for the Paleogene high-pressure belt. Sample S_A (Po@Valenza, S4 in Fig. 7), draining most of the Western Alps, and sample S_B (Tanaro@Rivarone, S5 in Fig. 7) draining the Ligurian Alps and the Argentera Massif, are linearly combined, and compared with sample S_{A+B} collected downstream of their confluence (Po@Cornale, S7 in Fig. 7). Because the average zircon fertility is lower upstream sample S_A (12.6 ppm) than upstream sample S_B (19.2 ppm), the sediment contribution from the Western Alps is underestimated if zircon fertility is not taken into account (62% instead of 71% - yellow star in Fig. 14C). A similar result is obtained in figure 14D, when an additional tributary is included in the calculation (Scrivia@Serravalle, F34 in Fig. 7).

The example 3 (Fig. 14E) illustrates a sediment budget for the entire Po basin. Grain-ages from the Paleogene alpine wedge (S_A), the Cretaceous wedge (S_B) and the Apennines (S_C) are linearly combined, and compared with the grain-age distribution in the Po delta. Results show that the zircon contribution to the Po delta possibly mirrors the differential zircon fertility in the eroded bedrock. Zircon fertility in the Alps, in fact, is one order of magnitude higher than in the Apennines (18-10 ppm vs. 3 ppm). As a consequence, the sediment contribution from the Apennines may remain undetected when analyzed using detrital zircon U-Pb data.

8.2. Examples based on the along-trunk sampling strategy

The sediment budgets in the NW Alps, illustrated in Fig. 15, are based on fission-track analyses of detrital apatites. Bedrock fission-track data in the NW Alps highlight the presence of two major fault-bounded blocks (Western and Eastern Blocks in Fig. 15A) juxtaposed along the Internal Houiller Fault (IHF in Fig. 15; Malusà et al., 2005). These blocks show distinct and not overlapping apatite fission-track ages (Fig. 15A), <10 Ma in the Western Block, and 10-35 Ma in the Eastern Block (Malusà et al., 2005; 2006 and references therein). Such an age structure, which allows us to perform sediment budgets according to the along-trunk approach, has been interpreted in the light of the orogen-scale right-lateral transpression affecting the NW Alps during the Neogene (Malusà et al., 2009b), leading to the relative uplift and preferred erosional exhumation of the Western Block relative to the Eastern Block (Fig. 15A).

Both the Dora Baltea River, flowing eastward towards the Po River, and the Arc River, flowing westward towards the Isère and Rhône Rivers (see Fig. 7), cut across this peculiar age structure. The thermochronological fingerprint of sediment samples collected along the Dora Baltea and Arc

Rivers faithfully mirrors the age structure found in bedrock (Fig. 15B). In the Dora Baltea River, both sample $S_{A'}$ (F12 in Fig. 7) collected along the Frontal Pennine Fault and exclusively derived from the Mont Blanc Massif, and sample $S_{A''}$ (F13 in Fig. 7) collected in correspondence of the Internal Houiller Fault, show a young age population at 6-7 Ma, which is consistent with the bedrock fission-track ages found in the Western Block (A in the map of Fig. 15B). This young population is associated downstream with an older age population at 15-20 Ma, consistent with the bedrock fission-track ages found in the Eastern Block (B in the map of Fig. 15B). At the closure section of the Dora Baltea catchment (sample S_{A+B}, F22 in Fig. 7), the older age population represents 57% of the total apatite contribution.

The same age populations are also observed in sediment samples from the Arc River (Fig. 15B). The Arc River sample collected upstream the Internal Houiller Fault (S_B, F19 in Fig. 7) displays an old age population at 15-20 Ma, derived from the erosion of the Eastern Block. This old population is associated downstream with a younger age population at 7-8 Ma, derived from the erosion of the Western Block. This young population represents 32% of the total apatite contribution in correspondence of the Frontal Pennine Fault (sample $S_{A+B'}$, F18 in Fig. 7), but its contribution increases to 71% immediately downstream of the External Massif, at the closure section of the mountain catchment (sample $S_{A+B''}$, F14 in Fig. 7). None of these samples show any correlation between grain age and grain size (Resentini and Malusà, 2012, their Fig. 6), which implies that the geochronological signature is not vulnerable to hydraulic sorting effects.

Given the area of each subbasin, the modal petrographic composition of the analyzed samples, and the annual sediment load at the closure section (see details in Resentini and Malusà, 2012), the map in Fig. 15C illustrates the distribution of inferred bedload erosion rates both under the assumption of constant mineral fertility (white boxes) and when the measured fertility is taken into account (yellow boxes). When apatite fertility is considered, bedload erosion rates are fully consistent along the orogen strike (Fig. 15C). They are on the order of 0.4-0.5 mm/a in the External Massifs (Belledonne and Mont Blanc), and ~0.1 mm/a both in the axial belt units of the Western Block and in the Eastern Block. Such an along-strike consistency of erosion rates is in agreement with the cylindrical tectonic framework depicted in Fig. 15A (Malusà et al., 2009b).

A comparison between the average Neogene erosion rates derived from bedrock fission-track data, and the Holocene bedload erosion rates derived from detrital thermochronology data, reveals a progressive westward shift of erosional foci, with erosion now concentrated in the External Massifs (Fig. 15D). Under the assumption of constant apatite fertility in the whole NW Alps, instead, modern erosion rates would be underestimated in the Belledonne Massif, but overestimated in the Mont Blanc Massif (Fig. 15C), and the resulting erosion pattern would be misleading.

Figures 12, 13, 14, 15

9. Extrapolation to the past

In ancient sedimentary successions, the abundace and potential preservation of mineral species is not only a function of mineral fertility and hydraulic and mechanical processes during transport, but also depends on the relative stability of different minerals to diagenetic dissolution (Morton, 1984; Andò et al., 2012). Mineral concentration measured in ancient sedimentary rocks cannot be used safely to estimate the mineral fertility in source rocks, because diagenetic dissolution makes any comparison with original detrital modes uncertain. Specifically, diagenesis may lead to a sharp decrease in dense mineral concentration in sediment, and a relative increase of ultrastable species such as zircon, tourmaline and rutile (see the diagenesis trend in Fig. 6B). Cemented sandstones also require either electric-pulse or disk-mill disaggregation before processing and, in the latter case, grain-size relationships are lost, and modelling with MinSORTING precluded.

However, using the geochronological fingerprint of specific minerals such as apatite or zircon as a provenance tool, as opposed to bulk sedimentary rocks, minimizes the effects of differing stabilities of minerals during diagenesis (Hietpas et al., 2011; von Eynatten and Dunkl, 2012). The approach to mineral fertility bias based on the analysis of modern sediments can thus be proficiently extrapolated to the past, whenever it can be reasonably assumed that the past mountain catchment was not markedly different from its present-day configuration. In the case of the Central Alps, the drainage network has been substantially stable since the Oligocene (Garzanti and Malusà, 2008), and the mineral fertility values measured on modern sediments (Fig. 11) could be extrapolated to the analysis of Oligo-Miocene turbidites now accreted in the Apennines (Fig. 7). A relative stability of the drainage network since the Pliocene, or even earlier, can be instead assumed for the more external units of the Alps or, in the Himalaya, for the Indus and Ganga-Brahmaputra drainage systems down to the Indus and Bengal Fans (Clift and Blusztajn, 2005).

Figure 15E illustrates an example of sediment budget applied to the Pleistocene of the NW Alps. In Pleistocene times, the drainage network of the Dora Baltea catchment was already stable, and substantially similar to its present-day configuration (Gianotti et al., 2008). We performed detrital apatite fission-track analysis on a Pleistocene glacifluvial deposit collected at the closure section of the Dora Baltea catchement (Dora Morta - Ivrea amphitheatre), and performed a sediment budget based on the along-trunk sampling strategy, using the mineral fertility values for the Western and Eastern Blocks previously measured in modern sediments. The analyzed Pleistocene sample shows two grain-age populations that faithfully mirror the bedrock ages found in the Western and Eastern Blocks, and with similar size as the populations provided by the analysis of

modern sediment (cf. sample S_{A+B} in Fig. 15B). We conclude that the erosion pattern derived from the analysis of the Pleistocene sample is substantially similar to the pattern observed today.

10. Conclusions

Detrital geochronology studies require a careful evaluation of the effects induced by hydraulic sorting and by the variable abundance of analyzed minerals in different parent rocks. Because the physical processes of settling and selective entrainment are known, the effects of size-density sorting of detrital grains can be modelled mathematically, and the selective entrainment effects in sediment can be easily detected by measuring its grain density. By contrast, the variable mineral fertility in parent rocks largely depends on their complex geological evolution, and the relationships between bedrock geology and mineral fertility are hardly predictable. As a consequence, a direct measurement of mineral fertility is required.

In this article, we have illustrated a quantitative approach to mineral fertility determination based on the analysis of modern sediments, and on the application of the basic principles of hydraulic sorting. This quantitative approach requires relatively minor modifications to routine separation procedures adopted in most detrital geochronology laboratories, and can be used to determine mineral fertility in bedrock of any age. Its application to the European Alps shows that apatite and zircon fertility may range over three orders of magnitude, thus representing the largest source of bias in detrital geochronology studies by far. In general terms, units consisting of chiefly metamorphic and plutonic rocks have higher apatite and zircon fertility than units largely consisting of sedimentary rocks, but major variations are also observed among tectonic units within the same paleogeographic domain.

Implications for detrital geochronology studies have been illustrated by examples from the European Alps according to different sampling strategies. In most of the cases, geological interpretations are strongly improved when mineral fertility is properly taken into account, not only in modern settings but also in ancient sedimentary successions.

Acknowledgments

D. Alami, R. Asti, M. Cordini, M. Fornara, M. Limoncelli, F. Lucini, C. Pellicioli, P. Piazza, G. Tango, F. Tangocci and M. Viganò contributed to mineral separation. F. Gianotti provided support during sampling of Pleistocene glacifluvial sediments. Insightful comments by two anonymous reviewers, fruitful discussions with M.L. Balestrieri, A. Carter, F. Guillot, S. Samson, P. Vermeesch, I.M. Villa, S. Andò, G. Vezzoli, and feedbacks from M. Horstwood, J. Košler, D. Rubatto, M. Tiepolo and other participants of the 2013 International School on zircon geochronology (Pavia), are gratefully acknowledged.

References

Amidon, W. H., Burbank, D. W., Gehrels, G. E., 2005a. Construction of detrital mineral populations: insights from mixing of U–Pb zircon ages in Himalayan rivers. Basin Research 17, 463–485.

Amidon, W.H., Burbank, D.W., Gehrels, G.E., 2005b. U–Pb zircon ages as a sediment mixing tracer in the Nepal Himalaya. Earth and Planetary Science Letters 235, 244-260.

Andersen, T., 2005. Detrital zircons as tracers of sedimentary provenance: limiting conditions from statistics and numerical simulation. Chemical Geology 216, 249-270.

Andò, S., Garzanti, E., Padoan, M., Limonta, M., 2012. Corrosion of heavy minerals during weathering and diagenesis: A catalog for optical analysis. Sedimentary Geology 280, 165-178.

Argand, E., 1911. Les nappes de recouvrement des Alpes occidentales et les territoires environnants, Mat. Carte Géol. Suisse, Bern, carte spec.

Bernet, M., Brandon, M.T., Garver, J.I., Molitor, B., 2004. Downstream change of Alpine Zircon Fission-Track Ages in the Rhône and Rhein Rivers. Journal of Sedimentary Research 74, 82-94.

Bernet, M., Garver, J.I., 2005. Fission-track analysis of detrital zircon. Reviews in Mineralogy and Geochemistry 58, 205-238.

Brandon, M.T., 1996. Probability density plot for fission-track grain-age samples. Radiation Measurements 26, 663-676.

Brewer, I.D., Burbank, D.W., Hodges, K.V., 2006. Downstream development of a detrital cooling-age signal: Insights from 40Ar/39Ar muscovite thermochronology in the Nepalese Himalaya. Special Paper of the Geological Society of America 398, 321-338.

Brown, E.T., Stallard, R.F., Larsen, M.C., Raisbeck, G.M., Yiou, F., 1995. Denudation rates determined from the accumulation of in situ-produced 10Be in the Luquillo experimental forest, Puerto Rico. Earth and Planetary Science Letters 129, 193-202.

Carrapa, B., Di Giulio, A., Wijbrans, J., 2004. The early stages of the Alpine collision: an image derived from the upper Eocene–lower Oligocene record in the Alps–Apennines junction area. Sedimentary Geology 171, 181-203.

Catanzariti, R., Ottria, G. Cerrina Feroni, A., 2002. Carta Geologico-Strutturale dell'Appennino Emiliano-Romagnolo. Tavole Stratigrafiche. SELCA Firenze, 92 pp.

Cawood, P.A., Nemchin, A.A., Freeman, M., Sircombe, K., 2003. Linking source and sedimentary basin: Detrital zircon record of sediment flux along a modern river system and implications for provenance studies. Earth and Planetary Science Letters 210, 259-268.

Cerrina Feroni, A., Ottria, G., Ellero, A., 2004. The northern Apennine, Italy: geological structure and transpressive evolution. In: U. Crescenti, d'Offizi, S., Merlino, S., Sacchi, L. (Eds), Geology of Italy. Special Volume Italian Geological Society, IGC 32 Florence-2004, 15–32.

Champagnac, J.D., Valla, P.G., Herman, F., 2014. Late-Cenozoic relief evolution under evolving climate: A review. Tectonophysics 614, 44-65.

Cheng, N.S., 1997. Simplified settling velocity formula for sediment particle. Journal of Hydraulic Engineering 123, 149–152.

Clift, P.D., Blusztjn, J., 2005. Reorganization of the western Himlayan river system after five million years ago. Nature 438, 1001-1003.

Dewey, J. F., Helman, M.L., Knott, S.D., Turco, E., Hutton, D.H.W., 1989. Kinematics of the western Mediterranean. Geological Society of London Special Publication 45, 265-283.

Dhuime, B., Hawkesworth, C.J., Storey, C.D., Cawood, P.A., 2011. From sediments to their source rocks: Hf and Nd isotopes in recent river sediments. Geology 39, 407-410.

Dickinson, W.R., 2008. Impact of differential zircon fertility of granitoid basement rocks in North America on age populations of detrital zircons and implications for granite petrogenesis. Earth and Planetary Science Letters 275, 80-92.

Dunkl, I., Székely, B., 2002. Component analysis with visualization of fitting—PopShare, a Windows program for data analysis. Goldschmidt Conference Abstracts 2002: Geochimica et Cosmochimica Acta 66/A, 201.

Elter, P., Catanzariti, R., Ghiselli, F., Marroni, M., Molli, G., Ottria, G., Pandolfi, L., 1999. L'Unità Aveto (Appennino settentrionale): caratteristiche litostratigrafiche, biostratigrafia, petrografia delle areniti ed assetto strutturale. Bollettino della Società Geologica Italiana 118, 41-63.

Engi, M., Bousquet, R., Berger, A., 2004. Explanatory notes to the map: Metamorphic structure of the Central Alps. Mitteilungen der Österreichischen Mineralogischen Gesellschaft 149, 157–173.

Fedo, C.M., Sircombe, K.N., Rainbird, R.H., 2003. Detrital zircon analysis of the sedimentary record. Reviews in Mineralogy and Geochemistry 53, 277-303.

Folk, R.L., Ward, W.C., 1957. Brazos River bar: a study in the significance of grain size parameters. Journal of Sedimentary Research 27, 3-26.

Garzanti, E., Andò, S., 2007a. Heavy Mineral Concentration in Modern Sands: Implications for Provenance Interpretation. In: Mange, M.A., Wright, D.T. (Eds), Heavy Minerals in use. Developments in Sedimentology 58, 517-545.

Garzanti, E., Andò, S., 2007b. Plate tectonics and heavy-mineral suites of modern sands. In Mange, M.A., Wright, D.T. (Eds), Heavy minerals in use. Developments in Sedimentology 58, 809-833.

Garzanti, E., Malusà, M.G., 2008. The Oligocene Alps: Domal unroofing and drainage development during early orogenic growth. Earth and Planetary Science Letters 268, 487-500.

Garzanti, E., Andò, S., Vezzoli, G., 2008. Settling equivalence of detrital minerals and grain-size dependence of sediment composition. Earth and Planetary Science Letters 273, 138-151.

Garzanti, E., Andò, S., Vezzoli, G., 2009. Grain-size dependence of sediment composition and environmental bias in provenance studies. Earth and Planetary Science Letters 277, 422-432.

Garzanti, E., Andò, S., France-Lanord, C., Vezzoli, G., Censi, P., Galy, V., Najman, Y., 2010. Mineralogical and chemical variability of fluvial sediments: 1. Bedload sand (Ganga–Brahmaputra, Bangladesh). Earth and Planetary Science Letters 299, 368-381.

Garzanti, E., Andó, S., France-Lanord, C., Censi, P., Vignola, P., Galy, V., Lupker, M., 2011. Mineralogical and chemical variability of fluvial sediments 2. Suspended-load silt (Ganga–Brahmaputra, Bangladesh). Earth and Planetary Science Letters 302, 107-120.

Garzanti, E., Resentini, A., Vezzoli, G., Andò, S., Malusà, M., Padoan, M., 2012. Forward compositional modelling of Alpine orogenic sediments. Sedimentary Geology 280, 149-164.

Gelati, R., Gnaccolini, M., 2003. Genesis and evolution of the Langhe basin, with emphasis on the latest Oligocene-Earliest Miocene and Serravallian. Atti Ticinensi Scienze della Terra 44, 3-18.

Gianotti, F., Forno, M.G., Ivy-Ochs, S., Kubik, P.W., 2008. New chronological and stratigraphical data on the Ivrea amphitheatre (Piedmont, NW Italy). Quaternary International 190, 123-135.

Glotzbach, C., van der Beek, P., Carcaillet, J., Delunel, R., 2013. Deciphering the driving forces of erosion rates on millennial to million-year timescales in glacially impacted landscapes: An example from the Western Alps. Journal of Geophysical Research: Earth Surface 118, 1491-1515.

Handy, M.R., Schmid, S.M., Bousquet, R., Kissling, E., Bernoulli, D., 2010. Reconciling plate-tectonic reconstructions of Alpine Tethys with the geological–geophysical record of spreading and subduction in the Alps. Earth-Science Reviews 102, 121-158.

Harrison, T.M., Watson, E.B., 1984. The behaviour of apatite during crustal anatexis: Equilibrium and kinetic considerations. Geochimica et Cosmochimica Acta 48, 1467-1477.

He, M., Zheng, H., Bookhagen, B., Clift, P., 2014. Controls on erosion intensity in the Yangtze River basin tracked by U-Pb detrital zircon dating. Earth-Science Reviews 136, 121-140.

Hietpas, J., Samson, S., Moecher, D., Schmitt, A.K., 2010. Recovering tectonic events from the sedimentary record: Detrital monazite plays in high fidelity. Geology 38, 167-170.

Hietpas, J., Samson, S., Moecher, D., Chakraborty, S., 2011a. Enhancing tectonic and provenance information from detrital zircon studies: assessing terrane-scale sampling and grain-scale characterization. Journal of the Geological Society of London 168, 309-318.

Hietpas, J., Samson, S., Moecher, D., 2011b. A direct comparison of the ages of detrital monazite versus detrital zircon in Appalachian foreland basin sandstones: Searching for the record of Phanerozoic orogenic events. Earth and Planetary Science Letters 310, 488-497.

Hodges, K.V., Ruhl, K.W., Wobus, C.W., Pringle, M.S., 2005. 40Ar/39Ar Thermochronology of Detrital Minerals. Reviews in Mineralogy & Geochemistry 58, 239-257.

Hubert, J.F., 1962. A zircon-tourmaline-rutile maturity index and the interdependence of the composition of heavy mineral assemblages with the gross composition and texture of sandstones. Journal of Sedimentary Research 32, 440-450.

Komar, P.D., 1984. Grain-size analyses of mica within sediments and the hydraulic equivalence of mica and quartz (Capistrano Formation, California). Journal of Sedimentary Petrology 54, 1379-1391.

Komar, P.D., 2007. The Entrainment, Transport and Sorting of Heavy Minerals by Waves and Currents, in: Mange,M.A., Wright, D.T. (Eds), Developments in Sedimentology 58, 3-48.

Komar, P.D., Li, Z., 1988. Applications of grain-pivoting and sliding analyses to selective entrapment of gravel and to flow-competence evaluations. Sedimentology 35, 681–695.

Le Roux, J.P., 2005. Grains in motion: A review. Sedimentary Geology 178, 285-313.

Malusà, M.G., 2014. Sediment budgets by detrital geochronology and new perspectives in understanding orogenic erosion (solicited). EGU General Assembly Conference Abstracts 16.

Malusà, M.G., Balestrieri, M.L., 2012. Burial and exhumation across the Alps–Apennines junction zone constrained by fission-track analysis on modern river sands. Terra Nova 24, 221–226.

Malusà, M. G., Polino, R., Zattin, M., Bigazzi, G., Martin, S., Piana F., 2005. Miocene to Present differential exhumation in the Western Alps: Insights from fission track thermochronology. Tectonics 24, TC3004.

Malusà, M.G., Philippot, P., Zattin, M., Martin, S., 2006. Late stages of exhumation constrained by structural, fluid inclusion and fission track analyses (Sesia–Lanzo unit, Western European Alps). Earth and Planetary Science Letters 243, 565-580.

Malusà, M.G., Zattin, M., Andò, S., Garzanti, E., Vezzoli, G., 2009a. Focused erosion in the Alps constrained by fission-track ages on detrital apatites. Geological Society of London Special Publication 324, 141-152.

Malusà, M.G., Polino, R., Zattin, M., 2009b. Strain partitioning in the axial NW Alps since the Oligocene. Tectonics 28, TC002370.

Malusà, M.G., Faccenna, C., Garzanti,E., Polino, R., 2011a. Divergence in subduction zones and exhumation of high pressure rocks (Eocene Western Alps). Earth and Planetary Science Letters 310, 21-32.

Malusà, M.G., Villa, I.M., Vezzoli, G., Garzanti, E., 2011b. Detrital geochronology of unroofing magmatic complexes and the slow erosion of Oligocene volcanoes in the Alps. Earth and Planetary Science Letters 301, 324-336.

Malusà, M.G., Carter, A., Limoncelli, M., Villa, I.M., Garzanti, E., 2013. Bias in detrital zircon geochronology and thermochronometry. Chemical Geology 359, 90-107.

Malusà, M.G., Danišík, M., Kuhlemann, J., 2015a. Tracking the Adriatic-slab travel beneath the Tethyan margin of Corsica-Sardinia by low-temperature thermochronometry. Gondwana Research in press. doi:10.1016/j.gr.2014.12.011

Malusà, M.G., Faccenna, C., Baldwin, S.L., Fitzgerald, P.G., Rossetti, F., Balestrieri, M.L., Danišík, M., Ellero, A., Ottria, G., and Piromallo, C., 2015b. Contrasting styles of (U)HP rock exhumation along the Cenozoic Adria-Europe plate boundary (Western Alps, Calabria, Corsica). Geochemistry, Geophysics, Geosystems 16(6), 1786-1824. doi: 10.1002/2015GC005767.

McLennan, S.M., Hemming, S., McDaniel, D.K., Hanson, G.N., 1993. Geochemical approaches to sedimentation, provenance, and tectonics. Geological Society of America Special Papers 284, 21-40.

Merle, O., Cobbold, P. R., Schmid, S., 1989. Tertiary kinematics in the Lepontine dome. Geological Society of London Special Publication 45, 113-134.

Moecher, D.P., Samson, S.D., 2006. Differential zircon fertility of source terranes and natural bias in the detrital zircon record: Implications for sedimentary provenance analysis. Earth and Planetary Science Letters 247, 252-266.

Morton, A.C., 1984. Stability of detrital heavy minerals in Tertiary sandstones of the North Sea Basin. Clay Minerals 19, 287-308.

Morton A.C., Hallsworth, C., 2007. Stability of detrital heavy minerals during burial diagenesis. In: Mange, M.A., Wright, D.T., (Eds.), Heavy Minerals in Use, Elsevier, Amsterdam, Developments in Sedimentology Series 58, 215-245.

Mutti, E., Papani, L., Di Biase, D., Davoli, G., Mora, S., Segadelli, S., Tinterri, R., 1995. Il bacino terziario epimesoalpino e le sue implicazioni sui rapporti tra Alpi e Appennino. Memorie di Scienze Geologiche 47, 217-244.

Najman, Y.M.R., Pringle, M.S., Johnson, M.R.W., Robertson, A.H.F., Wijbrans, J.R., 1997. Laser 40Ar/39Ar dating of single detrital muscovite grains from early foreland-basin sedimentary deposits in India: Implications for early Himalayan evolution. Geology 25, 535-538.

Pratten, N.A., 1981. The precise measurement of the density of small samples. Journal Of Materials Science 16, 1737-1747.

Reid, I., Frostick, L.E., 1985. Role of settling, entrainment and dispersive equivalence and of interstice trapping in placer formation. Journal of the Geological Society of London 142, 739-746.

Resentini, A., Malusà, M.G., 2012. Sediment budgets by detrital apatite fission-track dating (Rivers Dora Baltea and Arc, Western Alps). Geological Society of America Special Papers 487, 125-140.

Resentini, A., Malusà, M.G., Garzanti, E., 2013. MinSORTING: An Excel® worksheet for modelling mineral grain-size distribution in sediments, with application to detrital geochronology and provenance studies. Computers & Geosciences 59, 90-97.

Rittenhouse, G., 1943. Transportation and deposition of heavy minerals. Geological Society of America Bulletin 54, 1725-1780.

Rosenberg, C.L., 2004. Shear zones and magma ascent: A model based on a review of the Tertiary magmatism in the Alps. Tectonics 23, TC3002.

Rubey, W.W., 1933. The size distribution of heavy minerals within a water laid sandstone. Journal of Sedimentary Petrology 3, 3-29.

Saylor, J.E., Knowles, J.N, Horton, B.K., Nie, J., Mora, A., 2012. Mixing of source populations recorded in detrital zircon U-Pb age spectra of modern river sands. Journal of Geology 121, 17-33.

Schmid, S.M., Bernoulli, D., Fügenschuh, B., Matenco, L., Schefer, S., Schuster, R., Tischler, M., Ustaszewski, K., 2008. The Alpine-Carpathian-Dinaridic orogenic system: correlation and evolution of tectonic units. Swiss Journal of Geosciences 101, 139-183.

Schuiling, R.D., De Meijer, R.J., Riezebos, H.J., Scholten, M.J., 1985. Grain size distribution of different minerals in a sediment as a function of their specific density. Geologie en Mijnbouw 64, 199-203.

Silver, L.T., Williams, I.S., Woodhead, J.A., 1981. Uranium in granites from the southwestern United States: actinide parent–daughter systems, sites and mobilization. U.S. Department of Energy Open–File Repository GJBX–45.

Sircombe, K.N., Stern, R.A., 2002. An investigation of artificial biasing in detrital zircon U-Pb geochronology due to magnetic separation in sample preparation. Geochimica et Cosmochimica Acta 66, 2379-2397.

Slingerland, R., Smith, N.D., 1986. Occurrence and Formation of Water-Laid Placers. Annual Review of Earth and Planetary Sciences 14, 113-147.

Spear, F.S., Pyle, J.M., 2002. Apatite, monazite, and xenotime in metamorphic rocks. In: Kohn, M.J., Rakovan, J., Hughes, J.M. (Eds.), Phosphates: Geochemical, Geobiological, and Materials Importance 48, 293-335. Reviews in Mineralogy and Geochemistry, Mineralogical Society of America, Washington, D. C.

Spiegel, C., Kuhlemann, J., Frisch, W., 2007. Tracing sediment pathways by zircon fission track analysis: Oligocene marine connections in Central Europe. International Journal of Earth Sciences 96, 363-374.

Steck, A., Hunziker, J., 1994. The Tertiary structural and thermal evolution og the Central Alps – compressional and extensional structures in a n orogenic belt. Tectonophysics 238, 229-254.

Taylor, S.R., McLennan, S.M., 1985. The Continental Crust: Its Composition and Evolution. Blackwell, Oxford.

Taylor, S.R., McLennan, S.M., 1995. The geochemical evolution of the continental crust. Reviews of Geophysics 33, 241-265.

Tranel, L. M., Spotila, J. A., Kowalewski, M. J., Waller, C. M., 2011. Spatial variation of erosion in a small, glaciated basin in the Teton Range, Wyoming, based on detrital apatite (U-Th)/He thermochronology. Basin Research 23, 571–590.

Vermeesch, P., 2004. How many grains are needed for a provenance study? Earth and Planetary Science Letters 224, 441-451.

Vermeesch, P., 2013. Multi-sample comparison of detrital age distributions. Chemical Geology 341, 140-146.

von Blanckenburg, F., Kagami, H., Deutsch, A., Oberli, F., Meier, M., Wiedenbeck, M., Barth, S., Fischer, H., 1998. The origin of Alpine plutons along the Periadriatic Lineament. Schweizerische Mineralogische und Petrographische Mitteilungen 78, 55-66.

von Eynatten, H., Dunkl, I., 2012. Assessing the sediment factory: the role of single grain analysis. Earth-Science Reviews 115, 97-120.

Wittmann, H., von Blanckenburg, F., Kruesmann, T., Norton, K.P., Kubik, P.W., 2007. Relation between rock uplift and denudation from cosmogenic nuclides in river sediment in the Central Alps of Switzerland. Journal of Geophysical Research: Earth Surface 112, 2156-2202.

Zanchetta, S., Garzanti, E., Doglioni, C., Zanchi, A., 2012. The Alps in the Cretaceous: a doubly vergent pre-collisional orogen. Terra Nova 24, 351-356.

Zhang, J.Y., Yin, A., Liu, W.C., Lin, D., Grove, M., 2012. Coupled U-Pb dating and Hf isotopic analysis of detrital zircon of modern river sand from the Yalu River (Yarlung Tsangpo) drainage system in southern Tibet: Constraints on the transport processes and evolution of Himalayan rivers. Geological Society of America Bulletin 1 24, 1449-1473.

Zhao, L., Paul, A., Guillot, S., Solarino, S., Malusà, M.G., Zheng, T., Aubert, C., Salimbeni, S., Dumont, T., Schwartz, S., Zhu, R., Wang, Q., 2015. First Seismic Evidence for Continental Subduction beneath the Western Alps. Geology, 43. doi: 10.1130/G36833.1

CAPTIONS

Figure 1: Impact of mineral fertility on sediment budgets based on detrital geochronology, and on inferred erosion rates. Bell-shaped probability curves indicate grain-age distributions in subbasins A and B, which are combined downstream to form a polymodal grain-age distribution where *n* and *m* indicate the mineral contribution from each source. In case 1, fertility is equal in all subbasins, as assumed in most detrital geochronology studies. In case 2, fertility differs by one order of magnitude in different subbasins (this is a conservative assumption, because variability in mineral fertility may span over orders of magnitude). The impact of mineral fertility on inferred erosion patterns is remarkable: in case 1, erosion rates are higher in subbasin A than in subbasin B; in case 2, by contrast, erosion rates are much higher in subbasin B than in subbasin A.

Figure 2: Physical parameters controlling settling and selective entrainment of detrital grains.
A - Size relationship between quartz and settling-equivalent minerals of different densities (all of these spheres settle at 0.0267 m/s in freshwater). Differences in density correspond to differences in grain size: low-density minerals (e.g., quartz) are thus associated in sorted sediments with significantly smaller dense minerals (e.g., zircon and monazite); the difference in size between settling-equivalent minerals is called size shift, and is generally referred to quartz.
B – The settling velocity (v) of a detrital grain in a fluid reflects the balance between gravitational force (F_G) and drag resistance due to turbulence (F_T) and viscosity (F_V) (after Garzanti et al., 2008); the viscosity effect is negligible in wind-laid sands; D = grain diameter; g = gravity; δ_m = mineral density; δ_f = fluid density; η = fluid viscosity; C_D = drag coefficient

C - Selective entrainment of detrital grains (modified after Komar and Li, 1988). Coarser quartz grains are more easily entrained than smaller settling-equivalent zircon grains, because the former have a smaller pivoting angle (α), and project higher above the bed thus experiencing greater flow velocities and drag forces (F_D); v = current velocity (v_T, at level of grain's top; v_D, at level of effective drag force); ψ = sheltering factor (depending on the percentage of grain area exposed to fluid drag); C_L = lift coefficient; d_1, d_2 = distance from pivot point (P); other keys as in B.

Figure 3: Size-shift in bedload mineral grains.

A - Theoretical size-shift (relative to quartz) predicted for apatite and zircon in bedload sediments of increasing grain size according to the Cheng (1997)'s formula. Size-shifts in sand increase with grain size, from those predicted by the Stokes' law to those predicted by the Impact law (cf. Fig. 2B), and also increase with grain density (size shifts are higher for zircon than for apatite).

B – Example of size shifts observed for detrital minerals in bedload sand as compared to theoretical values provided by the Cheng (1997)'s formula (Ganga river, after Garzanti et al., 2009). The size-shift for zircon is greater than predicted, because sieving underestimates the size of prismatic grains. Note that size shifts observed for platy micas are systematically negative because of their slow, shape-controlled settling velocity (Komar et al., 1984; Le Roux, 2005).

C - Predicted (continuous lines) and observed (dashed lines) mineral distributions with grain-size under the assumption that mineral grains (quartz, apatite and zircon) are perfect spheres (from Resentini et al., 2013). The good fit between predicted and observed distributions confirms that grain shape has a minor impact on settling for these minerals.

Figure 4: Flowchart for the determination of mineral fertility in bedrock from the measurement of mineral concentration in sediment samples. Steps A0 to A10 (in black) imply only minor modifications to routine procedures adopted in most detrital geochronology laboratories. Steps B1-B2 (in gray) are complementary analyses not strictly required for mineral fertility determination. Laboratory facilities include: high-precision balance (steps A1, A6-A8), Riffle-type sample splitter and microsplitter (steps A1, A7), set of sieves and ultrasonic bath cleaner (step A1), hydrostatic balance (step A2), MinSORTING software (step A3), Gemeni shaking table (step A5), sodium polytungstate, densimeter, centrifuge and liquid nitrogen (step A5), hand magnet and Frantz magnetic separator (step A7), liquid diiodomethane (step A7), petrographic microscope (step A8).

The same separation procedure can be applied, with minor modifications, to get fertility maps for any mineral. Minerals other than zircon and apatite can be concentrated according to their densities by using sodium polytungstate at different degrees of dilution after step A6. Hydraulically equivalent minerals having different density and size, such as kyanite and zircon in the diamagnetic

fraction denser than 3.32 kg/dm^3, can be separated by microsieving after step A7. Monazite and xenotime can be recovered from the paramagnetic mineral fraction after step A7, using a pocket spectroscope applied to a petrography microscope.

Figure 5: Grain size distribution and suitable size windows to maximize mineral recovery.

A - Bulk sediment grain-size distribution (histogram and cumulative frequency curve), based on sieving at 1ϕ intervals, with dashed gray lines indicating the relevant distribution percentiles (ϕ_n) for the calculation of mean grain size (D_m), sorting (σ), and skewness (Sk) of the bulk sediment (Folk and Ward, 1957; see formulas to the right); vc, very coarse sand; c, coarse sand; m, medium sand; f, fine sand; vf, very fine sand.

B to **D** - Distribution of apatite, zircon and monazite in different grain-size classes as modeled with MinSORTING, using different mean grain size and sorting values and a typical subducted-axial-belt modal composition (Resentini et al., 2013). The thick black line indicates a hypothetical, fixed grain-size range (63-250 μm) chosen for mineral separation. In B (correct size window), all of the target mineral is concentrated in the chosen size window. In C (same size window in poorly sorted sample), nearly half of the mineral is lost in fractions finer or coarser than the selected size window. In D (incorrect size-window), the target mineral is completely lost during separation, despite its original presence in the sediment sample.

Fig 6: **Reference parameters for testing selective entrainment, and diagenetic effects in ancient sandstones**.

A - Reference grain density values and dense mineral concentrations; black squares = modal values; gray bars = value spread (compiled from Garzanti and Andò, 2007a; Garzanti et al., 2010; provenance according to Resentini et al., 2013).

SRD (Source Rock Density index - Garzanti and Andò, 2007a) is a proxy of the average density of the source rocks, measured as the weighted average density of extrabasinal terrigenous grains counted under a microscope. HMC (Heavy Mineral Concentration index - Garzanti and Andò, 2007a) is the weight percentage of total grains denser than 2.9 kg/dm^3 obtained after separation in sodium polytungstate, corrected under the microscope for intrabasinal and authigenic grains and for platy minerals settling slower than quartz (which are here removed by hydrodynamic pre-concentration during step A5).

Note that dense mineral concentration and grain density of upper crustal rocks are generally <10% and ~2.70±0.05 kg/dm^3, respectively; significantly higher values in sediment attest to hydraulic concentration of denser grains by selective entrainment ("field of placer deposits").

B - Diagenesis trend (based on heavy mineral suites from modern and ancient Alpine sediments - Garzanti and Andò, 2007b) and selective entrainment trend (based on heavy mineral suites from the Rosetta placer, Nile Delta - Garzanti et al., 2009) plotted on a ZTR vs HMC diagram. The ZTR index (Hubert, 1962) is the percentage of chemically ultrastable species (zircon, tourmaline, and rutile) among transparent heavy minerals. Both trends show a progressive increase in ZTR. However, selective entrainment produces a progressive HMC increase in placers, whereas diagenetic dissolution of unstable species produces a progressive HMC decrease in ancient sandstones (boxes show sandstone age). For this reason, detection of selective entrainment effects is not straightforward in ancient sandstones.

Figure 7: Sample location map (see supplementary Table S1 for further details). Main tectonic domains after Malusà et al. (2011a, 2015b); Lepontine isograds after Steck and Hunziker (1994); Engi et al. (2004). A, Adamello; AA, Aar; AR, Argentera; B, Bregaglia/Bergell; BE, Belledonne; C, Biella; DM, Dora Maira; EL, Epiligurian; GO, Gotthard; GP, Gran Paradiso; HO, Houiller; LB, Ligurian Briançonnais; LD, Lepontine dome; LI, Ligurian; MB, Mont Blanc; MO, Monferrato; MR, Monte Rosa; PE, Pelvoux; SL, Sesia-Lanzo; TPB, Tertiary Piedmont Basin; VO, Voltri.

Figure 8: Hydraulic control on mineral fertility quantification.

A - Apatite and zircon fertility values (samples F1 to F40), calculated according to the procedure in Fig. 4, show no correlation with mean grain size and sorting of analyzed samples. This excludes any major control of grain size parameters on the mineral fertility results.

B - Grain density values and dense mineral concentrations in samples F1 to F40 indicate negligible selective entrainment effects in samples analyzed for the assessment of mineral fertility. Grain density is sistematically ≤ 2.7 kg/dm^3, with slightly higher values in samples partly derived from lower crustal rocks (e.g., F21 and F22). Dense mineral concentration is mostly <10%. Note that sample F33 shows higher dense mineral concentration because the analyzed size window is not sufficiently representative of the sample as a whole (the sample fraction falling within the analyzed window is indicated in gray). This example shows why the analyzed size window must be centered around the mean grain size of the bulk sediment, in order to avoid any prominent influence of intrasample mineralogical variability on dense mineral concentration estimates.

C - Geochemistry of analyzed samples (further details in supplementary Table S3): elements chiefly hosted in ultradense minerals show concentrations close to UCC (Taylor and McLennan, 1985; 1995), apart from sample F33 (dashed line) largely including detrital grains derived from erosion of mantle rocks (VO in Fig. 7). No evidence of selective entrainment effects is thus provided by bulk-sediment geochemical analyses.

Figure 9: Replicated measurements of zircon and apatite concentrations. Differences observed in replicated measurements (right side of the diagrams) are orders of magnitude smaller than the variability in mineral fertility values documented in different parent bedrocks (left side of the diagrams). This confirms that the analysis of modern sediments provides a reliable tool for minimizing the mineral fertility bias in detrital geochronology. Keys - A: Dora Baltea modern sand samples (1, point bar deposit; 2, overbank deposit collected 4 km apart); B: paleo-Dora Baltea point bar deposits ascribed to different detrital pulses of Pleistocene age (1 and 2, Dora Morta quarry); C, modern sand samples from distinct distributary channels in the Po delta (1, Po@Barricata; 2, Po@Bonelli) (see main text and supplementary Table S4 for further details).

Figure 10: Comparison with upper thresholds provided by geochemical analyses. Measured zircon and apatite fertility values (black dots – thick red and blue lines, respectively) are systematically lower than the upper thresholds provided by geochemical analyses (gray dots – thin yellow line) assuming that Zr and P_2O_5 are exclusively host in zircon and apatite, respectively. The vertical distance between the thin and the thick gray lines is a measure of the amount of Zr and P_2O_5 found either in minerals other than zircon and apatite, or as inclusions in other mineral grains. Such a vertical distance is lowest for the Central Alps, and greatest for the Southern Alps and the Alps-Apennines transition zone.

Note that the vertical scale on the right side of the diagram is shifted with respect to the scale on the left side by a factor of 0.497 for zircon (zircon molecular weigth = 183, Zr atomic weight = 91) and by a factor of 0.454 for apatite (apatite molecular weight = 312, P_2O_5 molecular weight = 142) to take into account the atomic/molecular weight ratios.

Figure 11: Mineral fertility maps of the Alps. Dots indicate samples analyzed for mineral fertility determinations (F1-40 in Fig. 7), numbers are measured fertility values (in ppm) in each subbasin (black lines = basin boundaries). Values for the Dora Baltea and Arc subbasins are calculated using the formula in Appendix 1. Fertility ranges found in specific tectonic units (dashed-gray geological boundaries as in Fig. 7) are extrapolated outside the analyzed subbasins, and crosschecked using lowland river samples (S1-13 in Fig. 7). Consistency between independent measurements in subbasins draining the same tectonic unit points to a prominent geological control on mineral fertility.

Figure 12: Alternative sampling strategies for sediment budget calculations.

A - Confluence sampling: it requires at least three samples, two from major tributaries (S_A and S_B) and one from the trunk river downstream their confluence (S_{A+B}); this approach does not require independent information on bedrock age structure, and allows a direct measurement of mineral fertility in each subbasin. Modelled distributions (white squares in the cumulative probability

diagram) are based on a linear combination of grain-age distributions in major tributaries, and the best-fit solution is determined by comparison with the empirical grain-age distribution downstream the confluence (cumulative probability curve in black) using a statistic test for the goodness of fit (e.g., the $D_{n,n'}$ parameter of the Kolmogorov-Smirnov statistics; k_α is the critical value for a significance level α). Results are then corrected for mineraly fertility.

B - Along-trunk sampling: only two samples (S_A and S_{A+B}) are needed to unmix the geochronological signal and characterize two subbasins in terms of mineral fertility. Fertility in subbasin A (F_A) is directly measured, fertility in subbasin B (F_B) is instead calculated (see formula and Appendix 1). This approach can be employed when a river cuts across rock units with distinct and not overlapping age structure, as known independently (probability curves in red and blue to the left). The downstream grain-age distribution S_{A+B} is deconvolved into individual age components of size *m* and *n*. Results are then corrected for mineraly fertility.

Figure 13: Vulnerability test for hydraulic sorting and mechanical abrasion during transport (modified after Malusà et al., 2013). The Alpine detrital zircon U-Pb dataset is based on the analysis of modern river sands from the Po drainage; its application to sediment budgets is shown in Fig. 14.
A - Detrital zircon U-Pb age distribution (histograms and kernel density estimates) in different grain-size classes (fine sand, very fine sand and coarse silt; n = number of analyzed grains). Similarity between distributions is evaluated by the K-S method, comparing the maximal distance ($D_{n,n'}$) between cumulative frequency curves (top-right) with the critical value K_α for a 0.05 significance level. $V_{K\text{-}S}$ is the difference between $K_{0.05}$ and $D_{n,n'}$. Because $V_{K\text{-}S} > 0$, differences in the dataset are not statistically significant, and grain-age distributions are not vulnerable to hydraulic sorting effects.
B – Downstream variation in the relative abundance of U-rich grains in different U-Pb age populations. Such a relative abundance does not change across the plain, which indicates that metamict grains are not selectively destroyed by mechanical abrasion during fluvial transport.
C - Downstream variation in the relative abundance of rounded zircon grains in different U-Pb age populations. The percentages of rounded zircon grains do not change across the plain, which indicates that zircon shape is largely unaffected by mechanical abrasion during transport.

Figure 14: Zircon U-Pb sediment budgets in the Alps according to the confluence sampling strategy. Budgets are based on detrital zircon U-Pb data published in Malusà et al. (2013). The cumulative probability curves (modeled between 0 and 3 Ga) are only shown for the 0-1 Ga interval. The yellow star (in the $D_{n,n'}$ vs $\%S_A$ diagram) indicates sediment contribution after zircon fertility correction; other keys as in Fig. 12.

A – Sample location map; drainage boundaries (dashed lines) and External Massifs (pale gray areas) are also shown.

B – Sediment budget for the Lepontine dome: sediment contribution from the eastern subdome (Ticino, sample S_A) is strongly overestimated (44% instead of 12% - yellow star) if zircon fertility is not properly considered.

C – Sediment budget for the Paleogene high-pressure belt: sediment contribution from the Western Alps (sample S_A) is underestimated (62% instead of 71% - yellow star) if zircon fertility is not taken into account.

D – Same as in C, including an additional tributary draining the Apennines (Scrivia - sample S_C): its contribution is possibly underestimated, because fertility in the Scrivia catchment is very low (1.9 ppm).

E – On the scale of the entire Po basin, differential zircon fertility in bedrock is possibly mirrored by zircon contribution to the delta; because zircon fertility is one order of magnitude higher in the Alps than in the Apennines, sediment contribution from the Apennines may remain undetected.

Figure 15: Sediment budgets in the NW Alps according to the along-trunk sampling strategy.

A – 3D model of the NW Alps (from Malusà et al., 2015b). A and B indicate subbasins draining crustal block (Western and the Eastern) with distiguishable apatite fission-track ages (age diagram based on Malusà et al., 2005; 2006, and references therein). This age structure is ascribed to differential Neogene exhumation within the framework of orogen-scale dextral strike-slip (Malusà et al., 2009b). White arrows are proportional to Neogene exhumation rates inferred from bedrock thermochronological data, the dashed white line indicates the Dora Baltea drainage boundary. ET, External thrusts; FPF, Frontal Pennine Fault; IF, Insubric Fault; IHF, Internal Houiller Fault.

B – Deconvolution of detrital apatite fission-track age distributions from the Dora Baltea and Arc river trunks (black squares indicate sample locations). Main tectonic boundaries (thick black lines) in the shaded relief maps as in panel A. Subcatchments A (red) and B (blue) refer to the Western and Eastern Blocks, respectively, in panel A. Apatite fertilities are referred to the whole catchment upstream of each sample (modified from Resentini and Malusà, 2012).

C – Holocene bedload erosion rates in the NW Alps under the hypothesis of constant fertility (white boxes) and including measured fertilities in the calculation (yellow boxes). Drainage boundaries of subcatchments draining the Eastern Block (blue) and the Western Block (red and orange) as in panel B.

D - Westward shift of erosional focus in the NW Alps (cross-section as in panel A) based on a comparison between Neogene average erosion rates (top) and Holocene bedload erosion rates (bottom). The former are based on bedrock fission-track data (Malusà et al., 2005), the latter are based on detrital thermochronology data in modern sediments (Resentini and Malusà, 2012).

E - Example of sediment budget for the Pleistocene Dora Baltea catchment, using the mineral fertilities measured in modern sediments (cf. Fig. 11A). The analyzed sample (Dora Morta, Ivrea amphitheatre) shows two main grain-age populations consistent with bedrock ages found in the Western and Eastern Blocks, and with similar size as the populations found in modern sediments (cf. sample S_{A+B} in panel B). The erosion pattern derived from this Pleistocene sample is similar to the erosion pattern observed today.

Appendix 1. Assessment of mineral fertility for along-trunk sampling

For any composite catchment (x+y), formed by sub-basins x and y, with fertility F(x) and F(y), the total sediment load is given by:

$$\frac{\text{apatite}\,(x+y)}{F(x+y)} = \frac{\text{apatite}\,(x)}{F(x)} + \frac{\text{apatite}\,(y)}{F(y)} \qquad \text{(A1)}$$

If sub-basins x and y contribute for a proportion *m* and *n* to the total apatite load, then:

$$m + n = 1 \qquad \text{(A2)}$$

Sediment partitioning can be thus expressed as:

$$\frac{\text{Apatite}\,(x+y)}{F\,(x+y)} = \frac{m\text{Apatite}\,(x+y)}{F(x)} + \frac{n\text{Apatite}\,(x+y)}{F(y)} \qquad \text{(A3)}$$

Ratios in equation (A3) are equal to sediment load in each sub-basin. Such an equation can be used to retrieve apatite fertility F(y), provided that F(x) and F(x+y) are established by measuring apatite concentration in sediments, and that apatite proportions *m* and *n* are established by decomposition of grain-age distributions (Fig. 12B). This approach can be iteratively applied in the case of basins consisting of three or more sub-basins.

Biographies

Marco G. Malusà is a Researcher at the Department of Earth and Environmental Sciences - University of Milano-Bicocca. He received his MSc (1997) and his PhD (2004) from the University of Torino. He has been a Researcher at the CNR-IGG in Torino (2002-2006), and is now head of the Laboratory for Fission Track Analysis at the University of Milano-Bicocca (since 2007). His research interests include detrital geochronology and the geological evolution of Alpine orogenic belts.

Alberto Resentini is a post-doc researcher at the Laboratory for Provenance Studies, University Milano-Bicocca. He received his MSc (2007) and PhD (2010) from the University of Milano-Bicocca. His research mostly deals with ancient and modern detrital signatures in orogenic belts. His research also deals with physical and chemical processes affecting sediments, their geochronological signature, and with the statistical significance of large compositional datasets.

Eduardo Garzanti, Full Professor at the Department of Earth and Environmental Sciences, University of Milano-Bicocca, received his PhD (1987) from the University of Milano. His research focuses on various aspects of Himalayan geology, including Paleozoic history, opening of Neotethys, and paleotectonic evolution of Indian passive and Asian active margins prior to, during and after their Paleocene collision. He studies physical and chemical processes of sediment generation along divergent and convergent modern plate margins, and erosion and sediment transport in big Asian, African and Alpine rivers and deserts of Asia, Arabia and Africa.

Figure 1

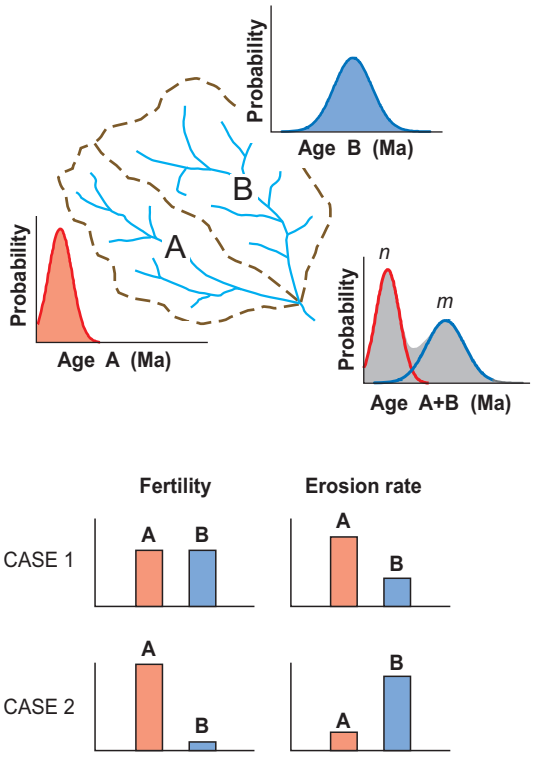
Probability
Age B (Ma)
B
A
Probability
Age A (Ma)
n
m
Probability
Age A+B (Ma)
Fertility
Erosion rate
CASE 1
A
B
A
B
CASE 2
A
B
B
A

Figure 2

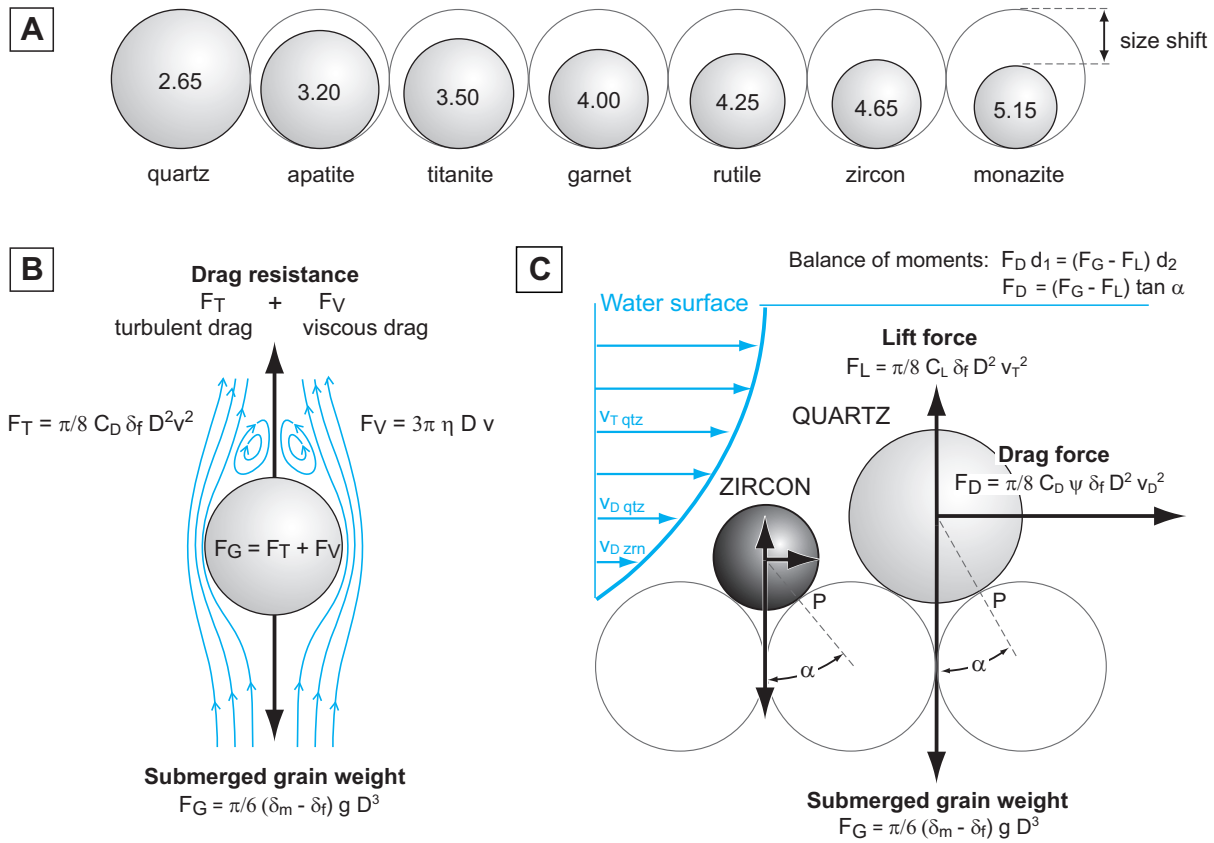
A
2.65
3.20
3.50
4.00
4.25
4.65
5.15
size shift
quartz
apatite
titanite
garnet
rutile
zircon
monazite
B
Drag resistance
FT + FV
turbulent drag
viscous drag
FT = π/8 CD δf D2v2
FV = 3π η D v
FG = FT + FV
Submerged grain weight
FG = π/6 (δm - δf) g D3
C
Balance of moments: FD d1 = (FG - FL) d2
FD = (FG - FL) tan α
Water surface
Lift force
FL = π/8 CL δf D2 vT2
QUARTZ
vT qtz
vD qtz
vD zrn
ZIRCON
Drag force
FD = π/8 CD ψ δf D2 vD2
P
P
α
α
Submerged grain weight
FG = π/6 (δm - δf) g D3

Figure 3

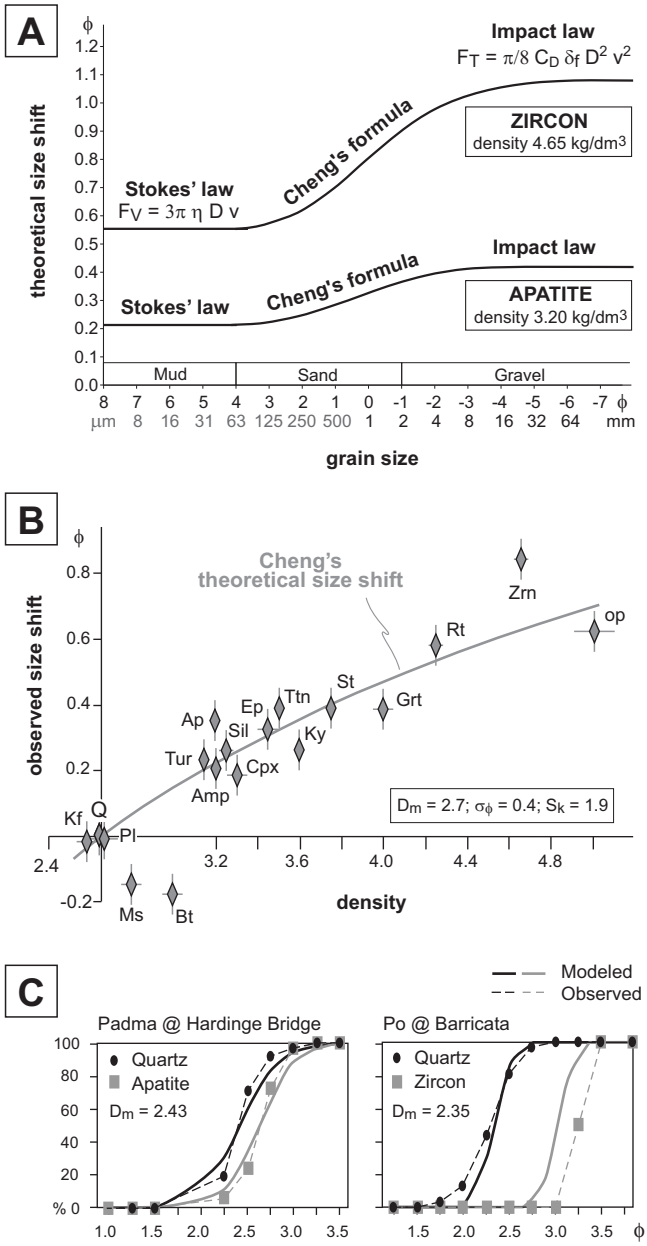
A
theoretical size shift
Impact law
$F_T = \pi/8\ C_D\ \delta_f\ D^2\ v^2$
ZIRCON
density 4.65 kg/dm3
Cheng's formula
Stokes' law
$F_V = 3\pi\ \eta\ D\ v$
Impact law
APATITE
density 3.20 kg/dm3
Cheng's formula
Stokes' law
Mud
Sand
Gravel
grain size
B
observed size shift
Cheng's theoretical size shift
Zrn
Rt
op
St
Ttn
Ep
Grt
Ap
Sil
Ky
Tur
Cpx
Amp
Kf
Q
Pl
Ms
Bt
$D_m = 2.7;\ \sigma_\phi = 0.4;\ S_k = 1.9$
density
C
Modeled
Observed
Padma @ Hardinge Bridge
Quartz
Apatite
$D_m = 2.43$
Po @ Barricata
Quartz
Zircon
$D_m = 2.35$

Figure 4

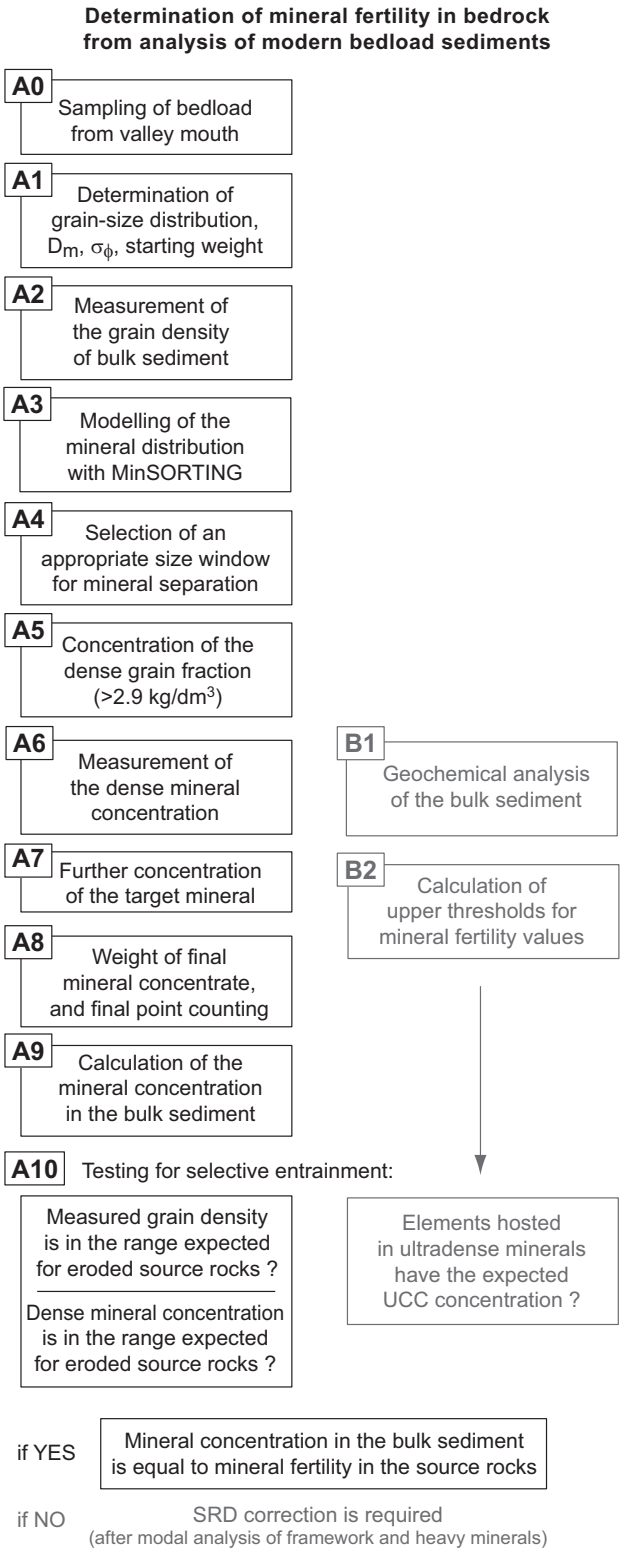
Determination of mineral fertility in bedrock from analysis of modern bedload sediments
A0
Sampling of bedload from valley mouth
A1
Determination of grain-size distribution, D_m, σ_ϕ, starting weight
A2
Measurement of the grain density of bulk sediment
A3
Modelling of the mineral distribution with MinSORTING
A4
Selection of an appropriate size window for mineral separation
A5
Concentration of the dense grain fraction (>2.9 kg/dm^3)
A6
Measurement of the dense mineral concentration
A7
Further concentration of the target mineral
A8
Weight of final mineral concentrate, and final point counting
A9
Calculation of the mineral concentration in the bulk sediment
B1
Geochemical analysis of the bulk sediment
B2
Calculation of upper thresholds for mineral fertility values
A10
Testing for selective entrainment:
Measured grain density is in the range expected for eroded source rocks ?
Dense mineral concentration is in the range expected for eroded source rocks ?
Elements hosted in ultradense minerals have the expected UCC concentration ?
if YES
Mineral concentration in the bulk sediment is equal to mineral fertility in the source rocks
if NO
SRD correction is required
(after modal analysis of framework and heavy minerals)

Figure 5

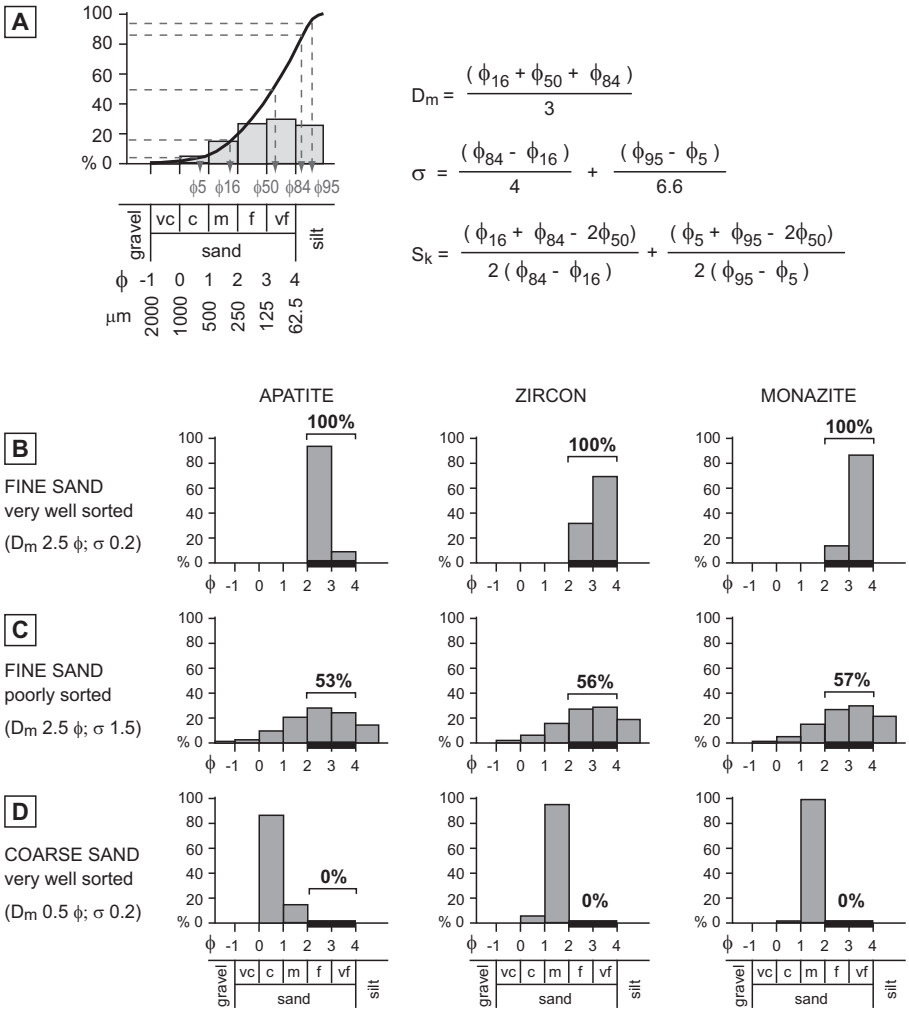
A
100
80
60
40
20
% 0
ϕ5 ϕ16 ϕ50 ϕ84 ϕ95
gravel
vc c m f vf
sand
silt
ϕ -1 0 1 2 3 4
μm 2000 1000 500 250 125 62.5
$D_m = \frac{(\phi_{16} + \phi_{50} + \phi_{84})}{3}$
$\sigma = \frac{(\phi_{84} - \phi_{16})}{4} + \frac{(\phi_{95} - \phi_5)}{6.6}$
$S_k = \frac{(\phi_{16} + \phi_{84} - 2\phi_{50})}{2(\phi_{84} - \phi_{16})} + \frac{(\phi_5 + \phi_{95} - 2\phi_{50})}{2(\phi_{95} - \phi_5)}$
APATITE
ZIRCON
MONAZITE
B
FINE SAND
very well sorted
(D_m 2.5 ϕ; σ 0.2)
100%
100%
100%
C
FINE SAND
poorly sorted
(D_m 2.5 ϕ; σ 1.5)
53%
56%
57%
D
COARSE SAND
very well sorted
(D_m 0.5 ϕ; σ 0.2)
0%
0%
0%

Figure 6

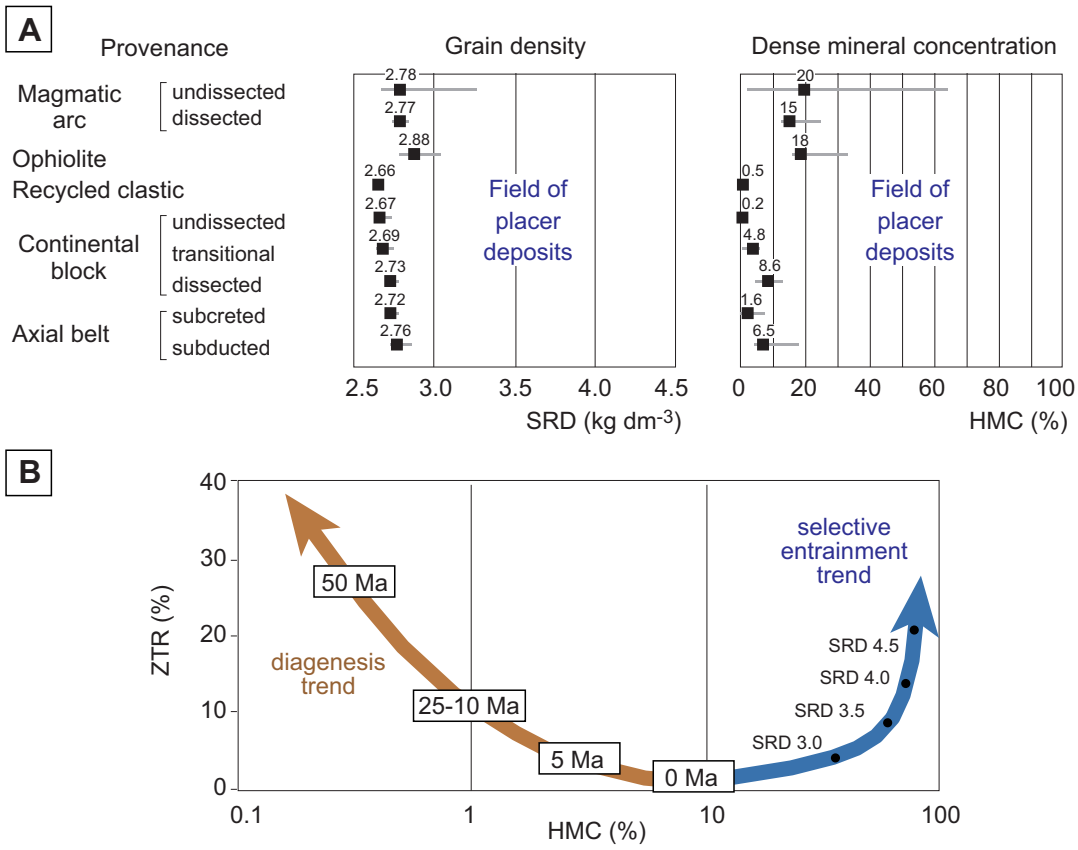
A
Provenance
Magmatic arc
undissected
dissected
Ophiolite
Recycled clastic
Continental block
undissected
transitional
dissected
Axial belt
subcreted
subducted
Grain density
2.78
2.77
2.88
2.66
2.67
2.69
2.73
2.72
2.76
Field of placer deposits
2.5 3.0 3.5 4.0 4.5
SRD (kg dm-3)
Dense mineral concentration
20
15
18
0.5
0.2
4.8
8.6
1.6
6.5
Field of placer deposits
0 20 40 60 80 100
HMC (%)

B
40
30
20
10
0
ZTR (%)
50 Ma
diagenesis trend
25-10 Ma
5 Ma
0 Ma
selective entrainment trend
SRD 4.5
SRD 4.0
SRD 3.5
SRD 3.0
0.1
1
10
100
HMC (%)

Figure 7

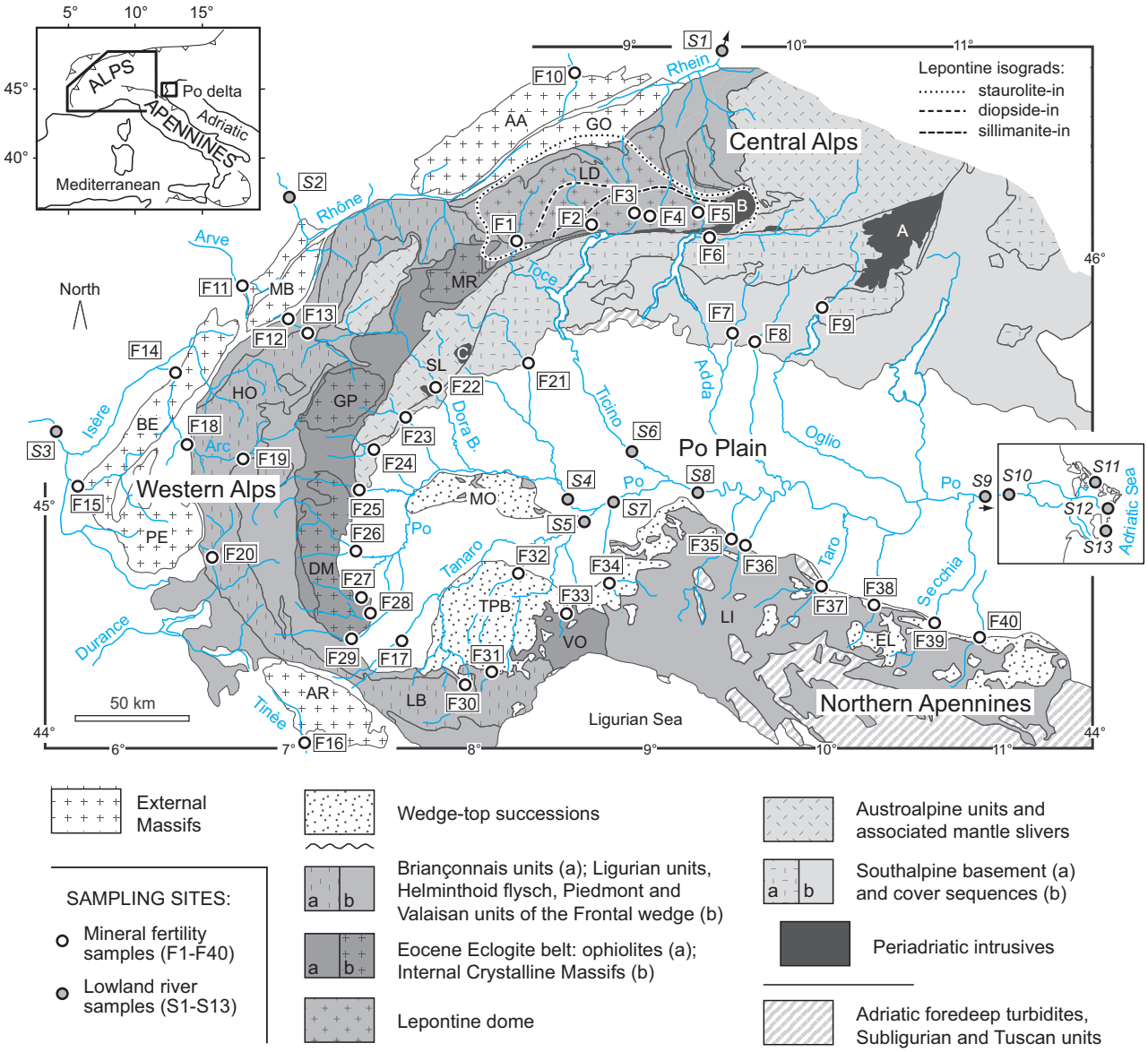

External Massifs

SAMPLING SITES:
- Mineral fertility samples (F1-F40)
- Lowland river samples (S1-S13)

Wedge-top successions

Briançonnais units (a); Ligurian units, Helminthoid flysch, Piedmont and Valaisan units of the Frontal wedge (b)

Eocene Eclogite belt: ophiolites (a); Internal Crystalline Massifs (b)

Lepontine dome

Austroalpine units and associated mantle slivers

Southalpine basement (a) and cover sequences (b)

Periadriatic intrusives

Adriatic foredeep turbidites, Subligurian and Tuscan units

Figure 8

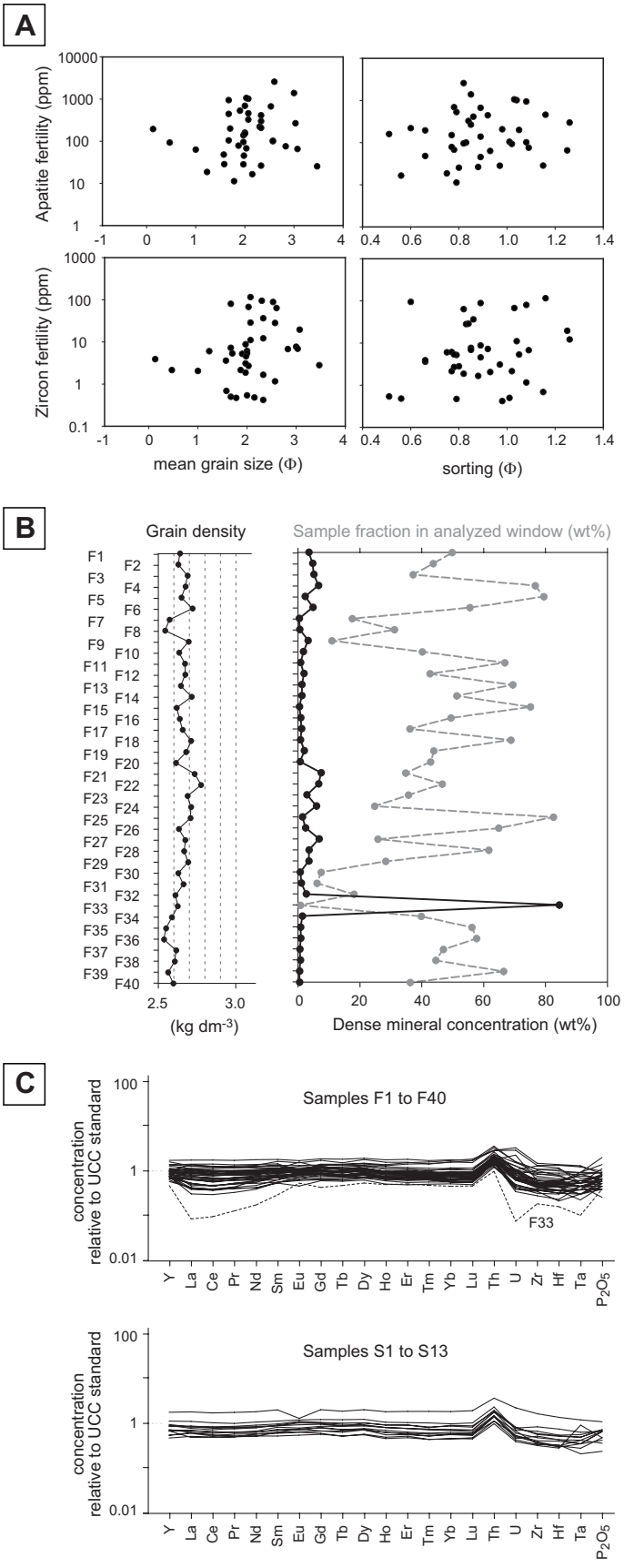
A
Apatite fertility (ppm)
Zircon fertility (ppm)
mean grain size (Φ)
sorting (Φ)
B
Grain density
Sample fraction in analyzed window (wt%)
(kg dm-3)
Dense mineral concentration (wt%)
C
Samples F1 to F40
F33
Samples S1 to S13
concentration relative to UCC standard
Y La Ce Pr Nd Sm Eu Gd Tb Dy Ho Er Tm Yb Lu Th U Zr Hf Ta P2O5

Figure 9

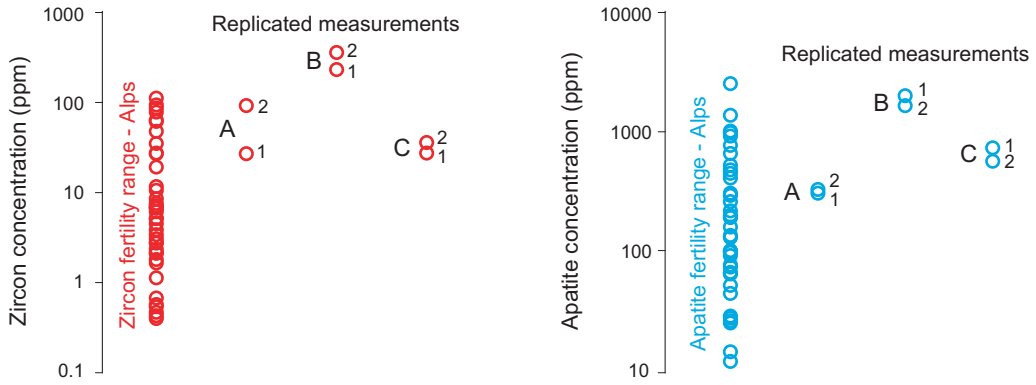
Zircon concentration (ppm)
1000
100
10
1
0.1
Zircon fertility range - Alps
Replicated measurements
A
B
C
Apatite concentration (ppm)
10000
1000
100
10
Apatite fertility range - Alps
Replicated measurements
A
B
C

Figure 10

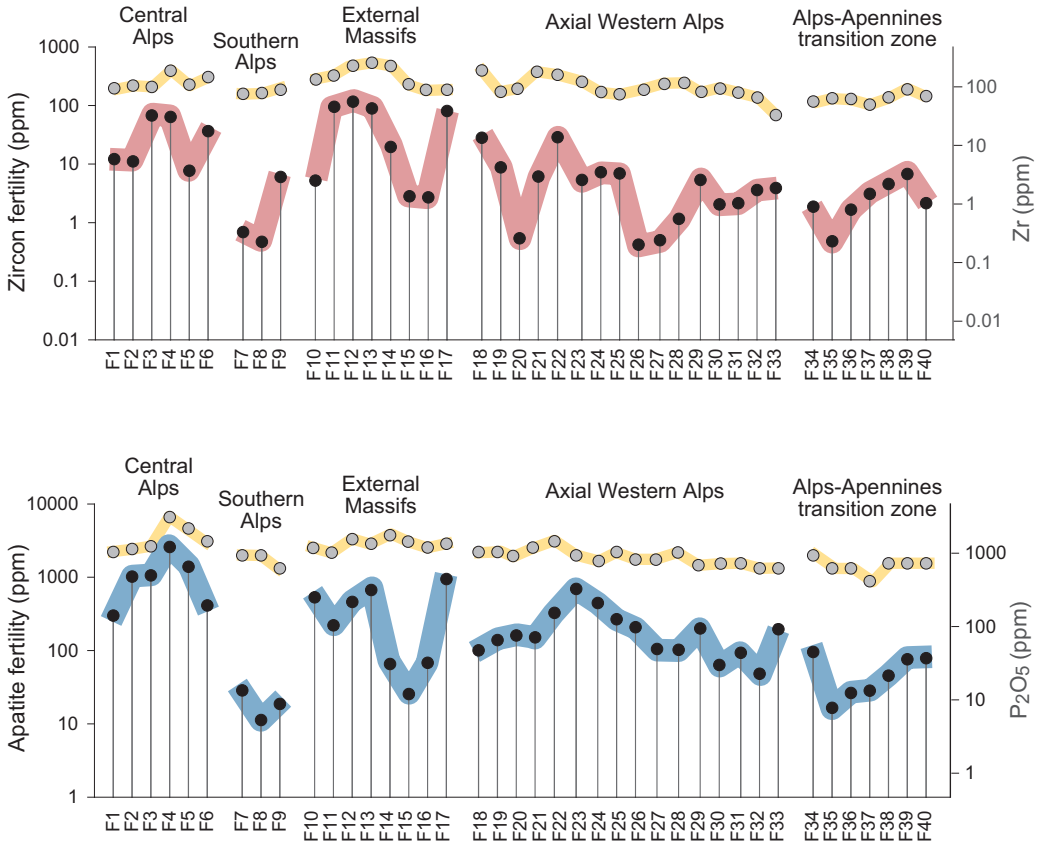
Central Alps
Southern Alps
External Massifs
Axial Western Alps
Alps-Apennines transition zone
Zircon fertility (ppm)
1000
100
10
1
0.1
0.01
Zr (ppm)
100
10
1
0.1
0.01
F1 F2 F3 F4 F5 F6 F7 F8 F9 F10 F11 F12 F13 F14 F15 F16 F17 F18 F19 F20 F21 F22 F23 F24 F25 F26 F27 F28 F29 F30 F31 F32 F33 F34 F35 F36 F37 F38 F39 F40
Central Alps
Southern Alps
External Massifs
Axial Western Alps
Alps-Apennines transition zone
Apatite fertility (ppm)
10000
1000
100
10
1
P2O5 (ppm)
1000
100
10
1
F1 F2 F3 F4 F5 F6 F7 F8 F9 F10 F11 F12 F13 F14 F15 F16 F17 F18 F19 F20 F21 F22 F23 F24 F25 F26 F27 F28 F29 F30 F31 F32 F33 F34 F35 F36 F37 F38 F39 F40

Figure 11

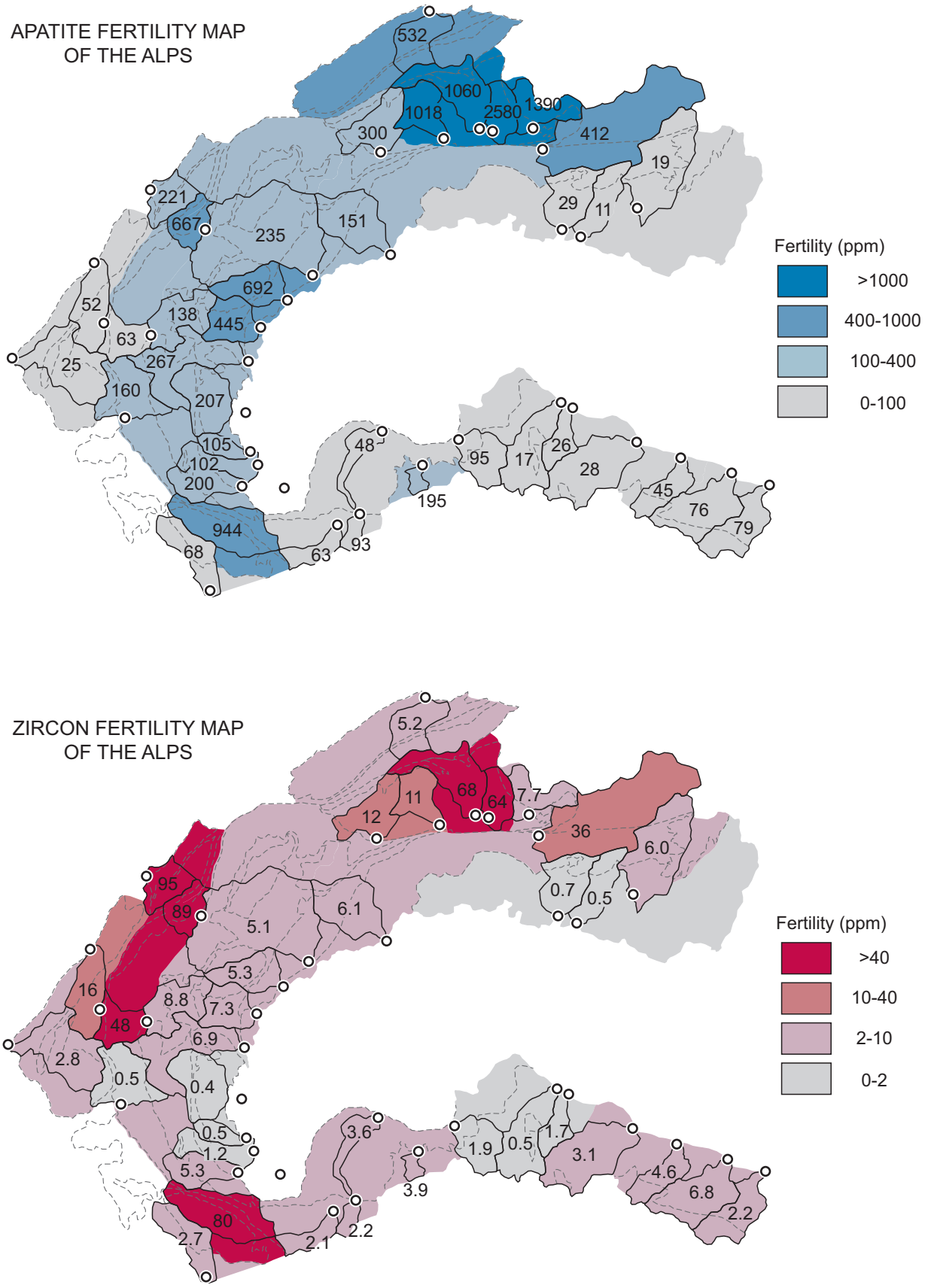
APATITE FERTILITY MAP
OF THE ALPS
532
1060
1018
2580
1390
412
300
19
29
11
221
667
235
151
692
52
138
445
63
267
25
160
207
105
102
200
944
68
63
93
48
195
95
17
26
28
45
76
79
Fertility (ppm)
>1000
400-1000
100-400
0-100
ZIRCON FERTILITY MAP
OF THE ALPS
5.2
68
64
7.7
11
12
36
6.0
0.7
0.5
95
89
6.1
5.1
5.3
16
8.8
7.3
48
6.9
2.8
0.5
0.4
0.5
1.2
5.3
80
2.7
2.1
2.2
3.6
3.9
1.9
0.5
1.7
3.1
4.6
6.8
2.2
Fertility (ppm)
>40
10-40
2-10
0-2

Figure 12

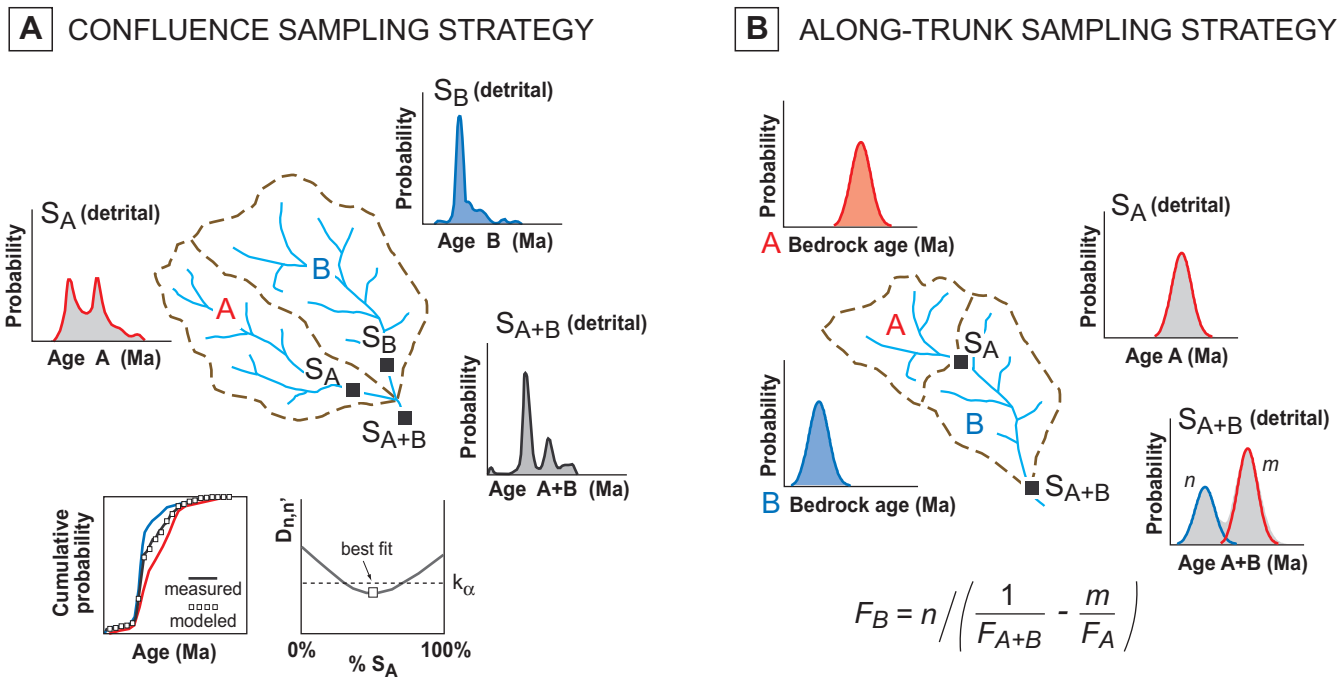
A CONFLUENCE SAMPLING STRATEGY
B ALONG-TRUNK SAMPLING STRATEGY
SB (detrital)
Probability
Age B (Ma)
SA (detrital)
Probability
Age A (Ma)
A
B
SB
SA
SA+B
SA+B (detrital)
Probability
Age A+B (Ma)
Cumulative probability
measured
modeled
Age (Ma)
Dn,n'
best fit
kα
0%
% SA
100%
Probability
A Bedrock age (Ma)
B Bedrock age (Ma)
SA (detrital)
Probability
Age A (Ma)
SA+B (detrital)
Probability
n
m
Age A+B (Ma)
$F_B = n / \left(\frac{1}{F_{A+B}} - \frac{m}{F_A} \right)$

Figure 13

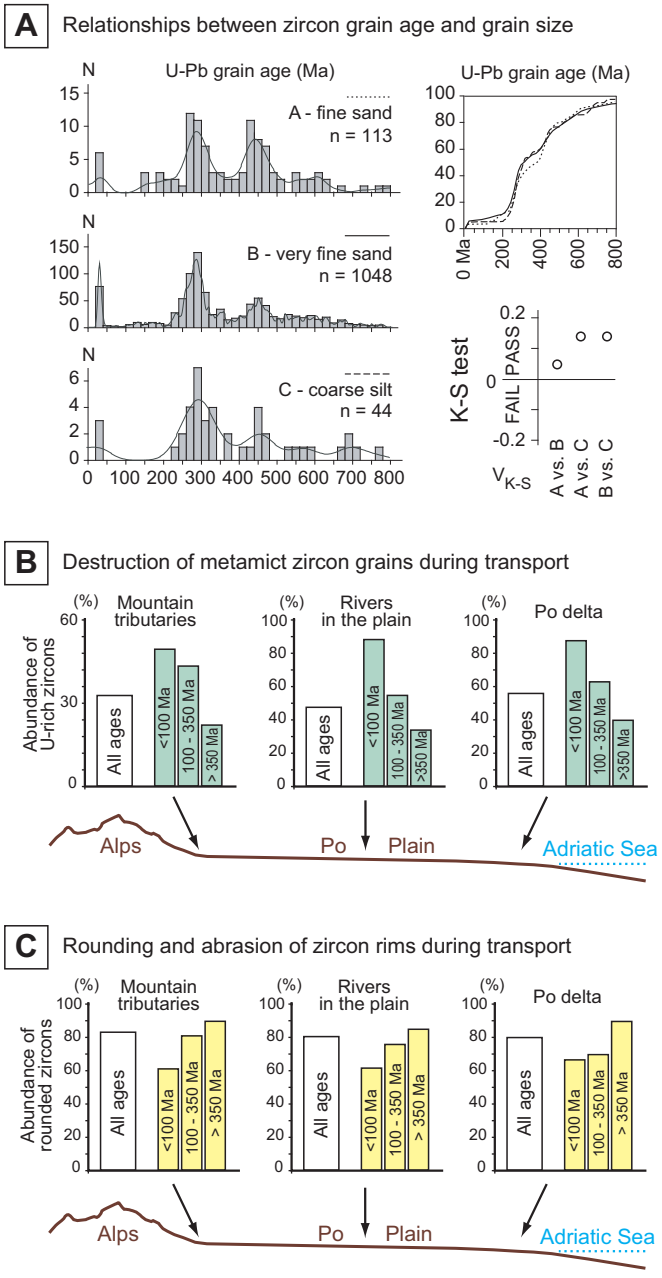
A
Relationships between zircon grain age and grain size
N
U-Pb grain age (Ma)
A - fine sand
n = 113
B - very fine sand
n = 1048
C - coarse silt
n = 44
0 100 200 300 400 500 600 700 800
U-Pb grain age (Ma)
0 Ma 200 400 600 800
K-S test
PASS
FAIL
V_{K-S}
A vs. B
A vs. C
B vs. C
B
Destruction of metamict zircon grains during transport
Abundance of U-rich zircons
(%)
Mountain tributaries
Rivers in the plain
Po delta
All ages
<100 Ma
100 - 350 Ma
> 350 Ma
Alps
Po
Plain
Adriatic Sea
C
Rounding and abrasion of zircon rims during transport
Abundance of rounded zircons

Figure 14

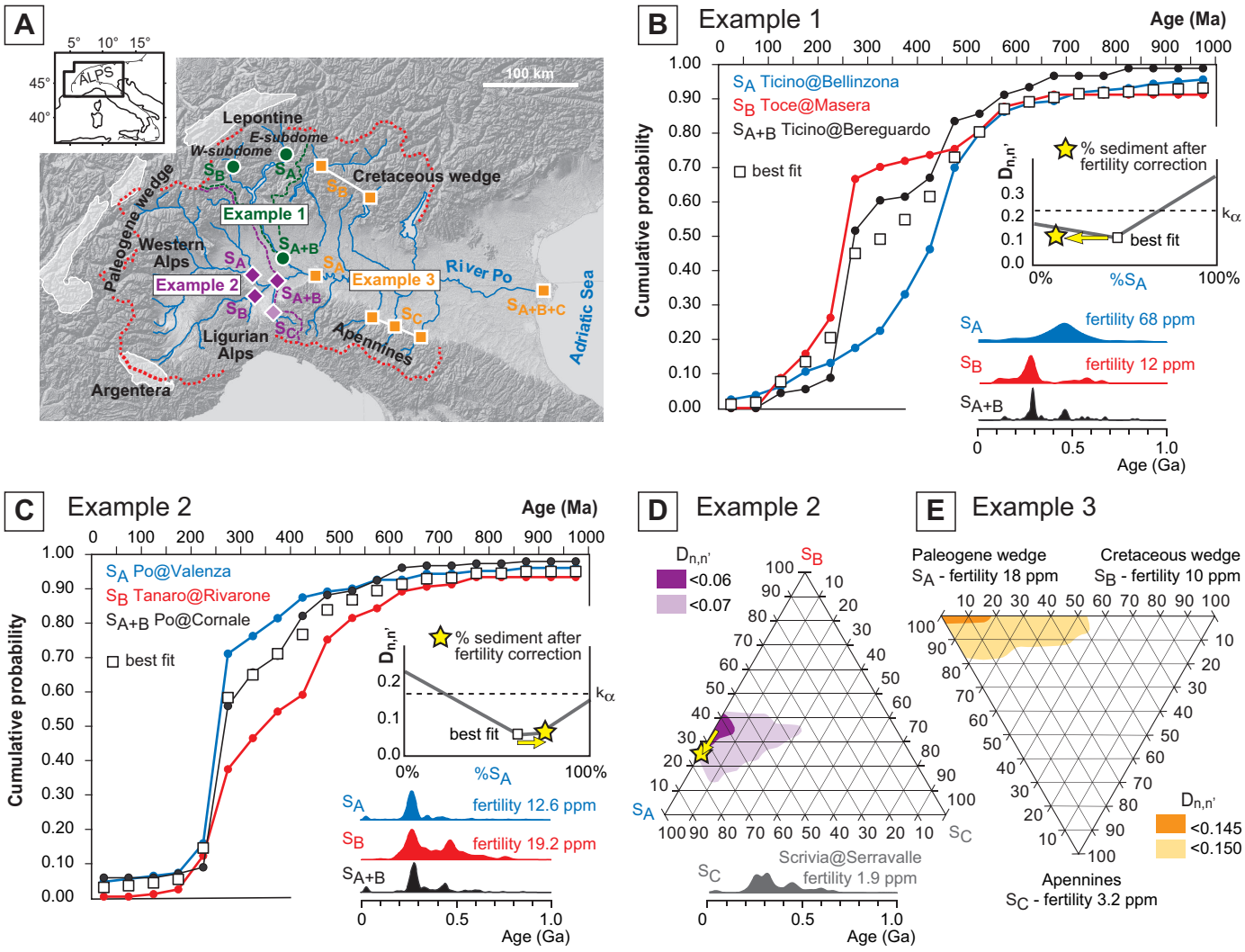
A
5° 10° 15°
45°
40°
ALPS
100 km
Lepontine
E-subdome
W-subdome
Cretaceous wedge
Example 1
Paleogene wedge
Western Alps
Example 2
Example 3
River Po
Adriatic Sea
Ligurian Alps
Apennines
Argentera
B
Example 1
Age (Ma)
Cumulative probability
SA Ticino@Bellinzona
SB Toce@Masera
SA+B Ticino@Bereguardo
best fit
% sediment after fertility correction
best fit
%SA
fertility 68 ppm
fertility 12 ppm
Age (Ga)
C
Example 2
Age (Ma)
SA Po@Valenza
SB Tanaro@Rivarone
SA+B Po@Cornale
best fit
% sediment after fertility correction
best fit
%SA
fertility 12.6 ppm
fertility 19.2 ppm
Age (Ga)
D
Example 2
<0.06
<0.07
Scrivia@Serravalle
fertility 1.9 ppm
Age (Ga)
E
Example 3
Paleogene wedge
SA - fertility 18 ppm
Cretaceous wedge
SB - fertility 10 ppm
<0.145
<0.150
Apennines
SC - fertility 3.2 ppm

Figure 15

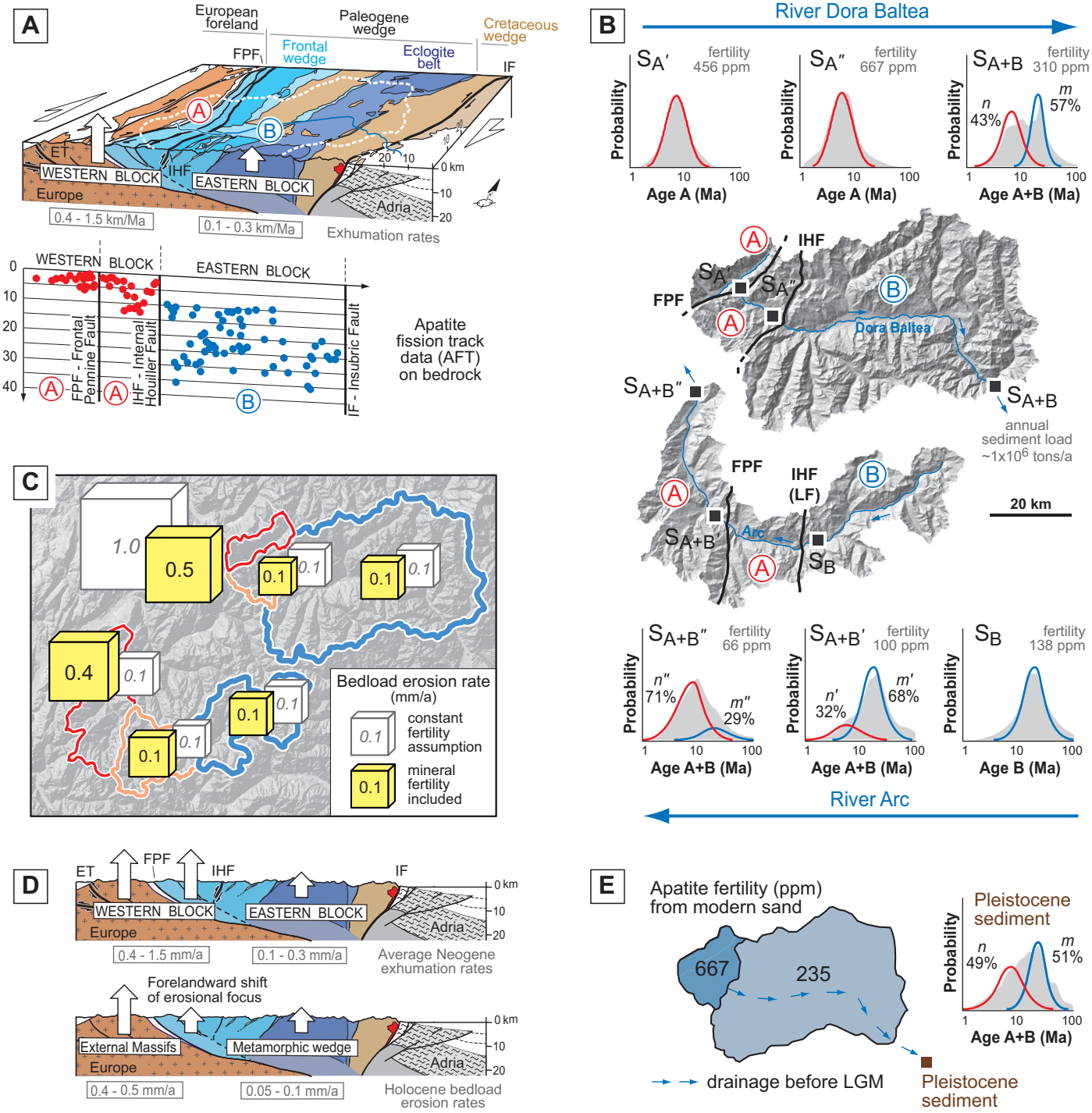
A
European foreland
Paleogene wedge
Cretaceous wedge
Frontal wedge
Eclogite belt
FPF
IF
ET
IHF
WESTERN BLOCK
EASTERN BLOCK
Europe
Adria
0.4 - 1.5 km/Ma
0.1 - 0.3 km/Ma
Exhumation rates
AFT age (Ma)
FPF - Frontal Pennine Fault
IHF - Internal Houiller Fault
IF - Insubric Fault
Apatite fission track data (AFT) on bedrock
B
River Dora Baltea
Probability
Age A (Ma)
Age A+B (Ma)
fertility 456 ppm
fertility 667 ppm
fertility 310 ppm
n 43%
m 57%
Dora Baltea
annual sediment load ~1x10^6 tons/a
20 km
Arc
fertility 66 ppm
fertility 100 ppm
fertility 138 ppm
n'' 71%
m'' 29%
n' 32%
m' 68%
Age B (Ma)
River Arc
C
Bedload erosion rate (mm/a)
constant fertility assumption
mineral fertility included
D
Average Neogene exhumation rates
Forelandward shift of erosional focus
External Massifs
Metamorphic wedge
0.4 - 0.5 mm/a
0.05 - 0.1 mm/a
Holocene bedload erosion rates
E
Apatite fertility (ppm) from modern sand
667
235
drainage before LGM
Pleistocene sediment
n 49%
m 51%